

REPORT DOCUMENTATION PAGE

Form Approved
OMB No. 0704-0188

Public reporting burden for this collection of information is estimated to average 1 hour per response, including the time for reviewing instructions, searching existing data sources, gathering and maintaining the data needed, and completing and reviewing this collection of information. Send comments regarding this burden estimate or any other aspect of this collection of information, including suggestions for reducing this burden to Department of Defense, Washington Headquarters Services, Directorate for Information Operations and Reports (0704-0188), 1215 Jefferson Davis Highway, Suite 1204, Arlington, VA 22202-4302. Respondents should be aware that notwithstanding any other provision of law, no person shall be subject to any penalty for failing to comply with a collection of information if it does not display a currently valid OMB control number. **PLEASE DO NOT RETURN YOUR FORM TO THE ABOVE ADDRESS.**

1. REPORT DATE (DD-MM-YYYY) 18-01-2011		2. REPORT TYPE Journal Article		3. DATES COVERED (From - To)	
4. TITLE AND SUBTITLE Experiments and Numerical Simulation of Mixing under Supercritical Conditions				5a. CONTRACT NUMBER	
				5b. GRANT NUMBER	
				5c. PROGRAM ELEMENT NUMBER	
6. AUTHOR(S) Thomas Schmitt and J. Rodriguez (CNRS, France); I.A. Leyva (AFRL/RZSA); and S. Candel (CNRS, France)				5d. PROJECT NUMBER	
				5f. WORK UNIT NUMBER 23080533	
7. PERFORMING ORGANIZATION NAME(S) AND ADDRESS(ES) Air Force Research Laboratory (AFMC) AFRL/RZSA 10 E. Saturn Blvd. Edwards AFB CA 93524-7680				8. PERFORMING ORGANIZATION REPORT NUMBER AFRL-RZ-ED-JA-2011-016	
9. SPONSORING / MONITORING AGENCY NAME(S) AND ADDRESS(ES) Air Force Research Laboratory (AFMC) AFRL/RZS 5 Pollux Drive Edwards AFB CA 93524-7048				10. SPONSOR/MONITOR'S ACRONYM(S)	
				11. SPONSOR/MONITOR'S NUMBER(S) AFRL-RZ-ED-JA-2011-016	
12. DISTRIBUTION / AVAILABILITY STATEMENT Approved for public release; distribution unlimited (PA #10731).					
13. SUPPLEMENTARY NOTES For publication in the Encyclopedia of Aerospace Engineering.					
14. ABSTRACT Supercritical conditions designate a situation where the working fluid pressure is above the critical point. Among these conditions, it is interesting to identify a transcritical range which corresponds to cases where the pressure is above the critical point, but the injection temperature is below the critical value. This situation is of special interest because it raises fundamental issues which have technological relevance in the analysis of flows in liquid rocket engines. This situation is here envisaged by analyzing the behavior of a nitrogen shear coaxial jet comprising an inner stream injected at temperatures close to the critical temperature and a coaxial flow at a higher temperature. Experiments are carried out both in the absence of external modulation and by imposing a large amplitude transverse acoustic field. Real gas Large Eddy Simulations are performed for selected experiments. The combination of experiments and calculations is used to evaluate effects of injector geometry and operating parameters. Calculations retrieve what is observed experimentally when the momentum flux ratio of the outer to the inner stream $J = (\rho_e u_e^2) / (\rho_i u_i^2)$ is varied. Results exhibit the change in flow structure and the development of a recirculation region when this parameter exceeds a critical value. The instantaneous flow patterns for different momentum flux ratios are used in a second stage to characterize the dynamical behavior of the flow in terms of power spectral density of velocity and density fluctuations. Results obtained under acoustic modulation provide insight on mixing enhancement of coaxial streams with a view of its possible consequences in high frequency combustion instabilities. It is shown in particular that the presence of strong acoustic modulations notably reduces the high density jet core length, indicating an increased mixing efficiency. This behavior is more pronounced when the jet is placed at the location of maximum transverse velocity fluctuations.					
15. SUBJECT TERMS					
16. SECURITY CLASSIFICATION OF:			17. LIMITATION OF ABSTRACT	18. NUMBER OF PAGES	19a. NAME OF RESPONSIBLE PERSON
a. REPORT	b. ABSTRACT	c. THIS PAGE			Dr. Douglas Talley
Unclassified	Unclassified	Unclassified	SAR	58	19b. TELEPHONE NUMBER (include area code) N/A

Experiments and numerical simulation of mixing under supercritical conditions

T. Schmitt¹, J. Rodriguez^{1,2}, I. A. Leyva² and S. Candel¹

¹EM2C, CNRS, Ecole Centrale Paris, 92295 Chatenay-Malabry, France,

^{1,2}AFRL/RZSA, Edwards AFB, CA. 93524, USA

February 3, 2011

Abstract

Supercritical conditions designate a situation where the working fluid pressure is above the critical point. Among these conditions, it is interesting to identify a transcritical range which corresponds to cases where the pressure is above the critical point, but the injection temperature is below the critical value. This situation is of special interest because it raises fundamental issues which have technological relevance in the analysis of flows in liquid rocket engines. This situation is here envisaged by analyzing the behavior of a nitrogen shear coaxial jet comprising an inner stream injected at temperatures close to the critical temperature and a coaxial flow at a higher temperature. Experiments are carried out both in the absence of external modulation and by imposing a large amplitude transverse acoustic field. Real gas Large Eddy Simulations are performed for selected experiments. The combination of experiments and calculations is used to evaluate effects of injector geometry and operating parameters. Calculations retrieve what is observed experimentally when the momentum flux ratio of the outer to the inner stream $J = (\rho_e u_e^2)/(\rho_i u_i^2)$

Approved for public release; distribution unlimited.

is varied. Results exhibit the change in flow structure and the development of a recirculation region when this parameter exceeds a critical value. The instantaneous flow patterns for different momentum flux ratios are used in a second stage to characterize the dynamical behavior of the flow in terms of power spectral density of velocity and density fluctuations. Results obtained under acoustic modulation provide insight on mixing enhancement of coaxial streams with a view of its possible consequences in high frequency combustion instabilities. It is shown in particular that the presence of strong acoustic modulations notably reduces the high density jet core length, indicating an increased mixing efficiency. This behavior is more pronounced when the jet is placed at the location of maximum transverse velocity fluctuations.

Nomenclature

α	Thermal expansion coefficient
β	Isothermal compressibility coefficient
λ	Thermal conductivity
μ	Dynamic viscosity
μ^t	Turbulent dynamic viscosity
ν^t	Turbulent kinematic viscosity
ω	Acentric factor
ρ	Density
ρ^*	Normalized density $(\rho - \rho_\infty)/(\rho_c - \rho_\infty)$
ρ_∞	Far field density

ρ_∞	Reservoir initial density
ρ_c	Time averaged centerline density
ρ_e	Outer jet injection density
ρ_i	Inner jet injection density
τ	Viscous-stress tensor
τ^t	SGS stress tensor
a, b, c	Coefficients for the Peng-Robinson equation of state
c_p	Constant pressure specific heat
c_v	Constant volume specific heat
C_w	WALE model constant
d_i	Inner jet diameter
E	Total energy
e_s	Internal energy
E_ρ^H	Spreading rate of the density profile
h_e	annular duct thickness
h_s	Enthalpy
J	Momentum flux ratio
l_i	Inner lip thickness
L_ρ	'Half Width at Half Maximum' of the density profile
$l_\rho^{0.1}$	$x_\rho^{0.1} - x_0$

$l_\rho^{0.5}$	$x_\rho^{0.5} - x_0$
$l_\rho^{0.99}$	$x_\rho^{0.99} - x_0$
l_u	$x_u - l_u$
p	Pressure
P_c	Critical pressure
R	Ideal gas constant
r	Specific gas constant
S	Density ratio
S	Symmetric part of the velocity-gradient tensor
s	Symmetric traceless part of the square of the velocity-gradient tensor
T	Temperature
T_c	Critical temperature
T_r	Reduced temperature
T_∞	Reservoir initial temperature
T_{aver}	Duration of the averaging procedure
T_e	Outer jet injection temperature
T_i	Inner jet injection temperature
U	Velocity ratio
u	Axial velocity
$u^* = u/u_e$	Normalized velocity

u_∞	Reservoir initial velocity
u_e	Outer jet injection velocity
u_i	Inner jet injection velocity
$x_\rho^{0.1}$	Axial centerline position where $\rho = 0.1(\rho_i - \rho_e) + \rho_e$
$x_\rho^{0.5}$	Axial centerline position where $\rho = 0.5(\rho_i - \rho_e) + \rho_e$
$x_\rho^{0.99}$	Axial centerline position where $\rho/\rho_i = 0.99$
x_u	Axial centerline position where axial velocity is minimum
\mathbf{q}^t	SGS heat flux vector
\mathbf{q}	Heat flux
\mathbf{v}	Velocity vector
\mathbf{w}	Vector of conservative variables
Pr^t	Turbulent Prandtl number
Re	Reynolds number
St^b	$(fu_e)/(d_i + l_i)$
St^e	$(fu_e)/h_e$
St^i	$(fu_i)/d_i$
St^l	$(fu_e)/l_i$

1 Introduction

Flows formed by coaxial injectors raise many fundamental issues. Such flows are also of practical relevance for high performance cryogenic liquid rocket engines (LREs). It is important to understand the basic processes taking place in these flows to improve the design methodology for future cryogenic LREs. Another potential application of research reported in this article lies in the area of combustion instability. It is known that mechanisms driving combustion oscillations result from the coupling between the injector flow, the combustion process and the chamber acoustic modes. The manner in which the inner and outer streams originating from a coaxial element interact with each other and with their surroundings may affect the temporal and spatial release of chemical energy within the chamber leading to undesired oscillations associated with a resonant acoustic motion. In most LREs, performance has been enhanced by augmenting the chamber pressure. Current LOx/H₂ engines like the SSME, Vulcain2 and RS-68 operate at values exceeding the critical pressure of their individual propellants. The inner jet, oxygen, is generally injected in a transcritical or liquid-like state (*i.e.* at a pressure higher than the critical value but at a temperature lower than the critical temperature) and it is surrounded by a higher-velocity hydrogen stream at supercritical temperature [72]. The inner fluid stream injected in a transcritical form evolves to a supercritical state as its temperature rises because of mixing and possibly combustion. Under such thermodynamic conditions, the system exhibits particular features that differ from those of a two-phase flow or of a pure gaseous injection. The objective of the present work is to compare experiments and simulations in which shear coaxial jet configurations are established at pressures above the critical point of the injected fluid, but at transcritical temperatures without and with acoustic excitation. For this study, nitrogen (N₂) is the only fluid used in the inner, outer and chamber flows.

At this point it is worth reviewing previous work dealing with supercritical injection. Starting with single round-jets, experiments have been carried out at AFRL (Air Force

Research Laboratory) [9] and DLR (Deutsches Zentrum für Luft- und Raumfahrt) [29, 41] (see also Oschwald *et al* [43] for a review up to 2006). Some recent investigations are reported by Segal and Polikov [61] and Roy and Segal [56]. These studies indicate that the liquid break-up and atomization mechanism which prevail at subcritical pressure are no longer observable because surface tension and latent heat of vaporization vanish at supercritical pressures [47]. The jet of fluid then dissolves in the ambient gas, with no evidence of droplets. The flow features “comb-like” structures at the edge of the dense stream, a type of pattern which is not observed at subcritical pressures [9]. The geometry of the flow is reminiscent of that of a variable density turbulent gas stream [9]. This behavior has been confirmed by experimental measurements of visual spreading rates in the initial region which are found to be consistent with theoretical growth rate expressions for incompressible variable-density turbulent mixing layers. Quantitative measurements of density [4, 41, 29], spreading rate and axial decay coefficients obtained by DLR [43, 40] using spontaneous Raman scattering also convey the same type of information.

Coaxial injection is investigated by several researchers at AFRL [14, 13, 25, 24, 55, 54] who examine the single-species case, and by Mayer and Smith [30] who examine a stream of nitrogen injected at low temperature (high density) surrounded by a high velocity stream of moderate temperature helium. Quantitative measurement of species density are reported by Oschwald *et al* [42] for a coaxial nitrogen / hydrogen injection, using spontaneous Raman Scattering. When compared with the round jet configuration, a strong reduction of the jet density potential core length is observed [43]. For shear coaxial jets, it has been found that the momentum flux ratio between the outer stream and the inner jet ($J = (\rho_e u_e^2)/(\rho_i u_i^2)$) is of major importance for the mixing efficiency [22, 69]. It has also been found that combustion is more stable and more efficient at high values of this quantity [5]. Different flow regimes may be obtained by varying this ratio [51] and that the inner jet core length decreases as the momentum flux ratio increases [13, 25].

The dynamics of coaxial transcritical jets is of interest for the study of combustion in-

stability. This can be examined by considering the interaction of acoustic waves with transcritical flows and its influence on mixing efficiency. The effect of an acoustic modulation on a single round jet at sub- and supercritical pressure is investigated by Chehroudi and Talley [8] who find that effects on the jet structure are more profound in the subcritical case. The impact of the modulation is reduced as the initial jet velocity is augmented. The impact of acoustics on a non-reacting shear coaxial jet has been investigated experimentally by Leyva and Rodriguez [25, 24, 55, 54]. They have assessed the effects of acoustics on the jet by measuring the spreading angle of the inner and outer jets and the length of the inner jet before its first break-up. It has been found that the injector geometry has an effect on the susceptibility of the coaxial flows to acoustic modulation. For the injector geometry studied here, acoustics have a measurable effect on the reduction of the inner jet dark core length for an intermediate value of J at pressures varying from 1.5 to 5.0 MPa. Reactive cases were also experimentally investigated (see [5, 19, 67, 64, 65] for example, and [53, 32] for acoustically modulated cases) but will not be detailed here since they are out of the scope of the present article.

The numerical modeling of such complex flows has been considered more recently by various groups. It is first noted that in the transcritical range, thermodynamic properties notably differ from those of a perfect gas and cannot be accurately represented with the standard perfect gas (PG) equation of state (EOS). Thermodynamics and “real-gas” (RG) EOS are required [47, 15, 71]. Cubic equations of state are generally used to this purpose [37], but more precise (and numerically expensive) equations may also be employed [71]. This issue and the modeling of transport properties are extensively reviewed in [1], [37], [31] and [2].

The models described in the previous studies are used in various calculations. Mixing at supercritical pressure is studied with direct numerical simulation in a mixing layer configuration, to show the role of density gradients on the global layer stability and turbulence characteristics and the strong effect on the molecular mixing of the reduced species diffusion near critical conditions [2]. This highlights the need for appropriate subgrid-scale

models for Large Eddy Simulation (LES) under supercritical pressure conditions [63, 68]. A few large eddy simulations (LES) have been performed under transcritical conditions. An extensive review of non-reacting LES in the period ending in 2006 can be found in Zong et al. [76]. A single nitrogen round jet was studied by Zong [74, 73] and recently by Schmitt *et al* [59]. Again, the stabilizing effect of the density gradient, and its role on turbulent energy redistribution along the mixing layer was identified [74]. Shear coaxial injection of oxygen and methane has also been simulated by Zong and Yang [75]. This has been continued by considering a non-reactive coaxial injector submitted to acoustic modulations [26] where a significant reduction of the jet intact core length is observed when acoustic perturbations are present.

One also notes that LES have been used for reactive cases at supercritical pressures. Shear coaxial jet flames were investigated by Oefelein [37, 38], Oefelein and Yang [36], Zong and Yang [77], Matsuyama *et al.* [28], Masquelet *et al.* [27] and Schmitt *et al.* [57]. The problem is also considered in the Reynolds Average Navier-Stokes (RANS) framework (see for example [16], [11] or [49]).

The present investigation focuses on the mixing behavior in the flow originating from a shear coaxial injector in the absence or in the presence of external acoustic modulation. Three operating points are considered corresponding to different momentum flux ratios. The coaxial jet geometry corresponds to a thick inner jet post (the wall which separates the inner and outer streams in the coaxial configuration has a thickness of the order of the jet diameter). In this article each case is defined by the chamber pressure, the momentum flux ratio, and the coaxial jet geometry which is fixed in the present study. The main components of the experimental facility are reviewed in section 2. Balance equations and models used in the simulations are briefly described in section 3. The definition of the computational domain and other numerical aspects are considered in section 4. The influence of the momentum flux ratio is examined in section 5. Results obtained are used to examine the dynamics of the flow and identify the spectral content in the various regions. Effects of a transverse acoustic modulation are investigated in section 6.

2 Experimental configuration

The experimental work described in this article was carried out at the Supercritical Cryogenic Test Facility (EC-4) of the Air Force Research Laboratory at Edwards Air Force Base, California. The facility features a test chamber that can achieve pressures over 5 MPa and cryogenic injection at temperatures below 120 K. The photograph in Fig. 1(a) shows the main test chamber and several key components of the facility. A schematic view of the test chamber is provided in Fig. 1(b). The facility was used to obtain a shear coaxial jet flow where the inner jet was cooled down to be denser than the outer jet under typical combustion chamber pressures, resembling conditions found in practice where the inner jet oxidizer is injected at a significantly lower temperature compared to that of the outer jet stream. A second equally important objective was to include the capability to perform acoustic forcing. When this was achieved the coaxial jet flow parameters were varied and the coaxial jet behavior was observed with and without acoustic excitation.

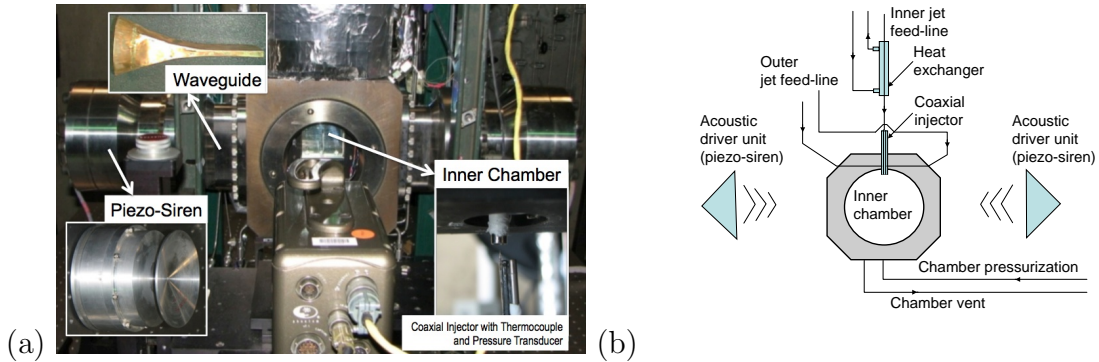


Figure 1: (a) Photograph of the main test chamber and key instrumentation of EC4, the supercritical cryogenic facility at AFRL, Edwards AFB. (b) Flow diagram of the test chamber and its vicinity.

To run a test, a laboratory-wide high pressure gaseous nitrogen supply was fed into the inner and outer flow lines of the coaxial jet and the flow rates adjusted to correspond to those of the desired test conditions. The mass flow rates through the inner and outer jets were measured with Porter mass flow meters (models 122 and 123-DKASVDAA). The

same gaseous nitrogen supply used for the coaxial jet was also employed to increase the pressure in the test chamber and achieve the required level, which was measured with a Stellar 1500 transducer. The jet temperatures were controlled by adjusting the flow rates of liquid nitrogen through the heat exchangers placed on the feed lines. Densities of the two jets were deduced from the measured temperatures and pressure using the National Institute of Standards and Technology's thermophysical properties of fluid systems online database [23]. These values in conjunction with the mass flow rate data provided the injection velocities and the corresponding Reynolds numbers, velocity and momentum flux ratios. Several thermocouples were used across the heat exchanger and in other locations to keep track of the conditions of the flow in order to maintain the required flow properties for each test case. Appendix A provides a summary of the operating conditions achieved for all cases reported in the present article. Two images of the shear coaxial injector can be seen in Fig. 2. The first, Fig. 2(a), gives a full view before assembly and the second, Fig. 2(b) shows a plane view of the end section. The inner jet diameter is $d_i = 0.51$ mm. The outer jet has an inner diameter of 1.59 mm and outer diameter of 2.42 mm. The injector outer diameter was 3.18 mm. The length to inner diameter ratio was 100 for the inner jet and 34 for the outer jet based on the hydraulic diameter. The coaxial injector was installed so that the inner and outer jets were nominally concentric. The inner jet exit plane was recessed by 0.3 mm from the outer jet exit plane. This recess length was chosen to mimic realistic coaxial jet configurations used in practice.

The coaxial injector was placed in an inner chamber within the main test chamber. This unit was protruding into the chamber by 5 mm through a 17 mm in diameter central orifice in the top wall. This inner chamber was created to augment the level of acoustic modulation acting on the coaxial flow. The inner chamber had a height of 6.6 cm, a width of 7.6 cm and a depth of 1.3 cm. The flow was exhausted through another orifice at the center of the bottom wall.

Injection temperatures were measured with unshielded traveling type E thermocouples with a bead diameter of 0.1 mm. The accuracy of the thermocouples used in the study was

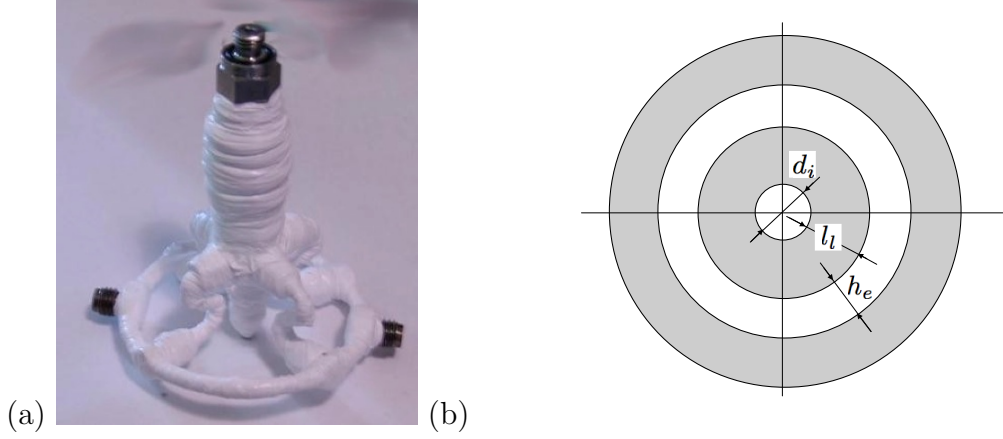


Figure 2: (a) Photograph of the shear coaxial injector used in this study. (b) Exit plane view of the injector.

checked with an RTD and found to be within 1 K. A miniature pressure transducer (Kulite Semiconductor Products, models CCQ-062-1000A and CCQ-093-750A) was placed next to the thermocouple using a small metallic post for support, and recorded pressure fluctuations at a sampling frequency of 20 kHz. These pressure transducers having an absolute pressure range of either 6.9 MPa or 5.2 MPa, respectively were used to scan the wavefield induced by the acoustic driver units prior to flow experiments.

The coaxial jet structure was observed with backlighting (shadowgraph) imaging. The flow was illuminated with a light source (Newport variable power arc lamp set at 160W or 300W) and the transmitted light was recorded with a Phantom v7.1 high-speed camera capable of recording up to 160,000 frames per second at a resolution of 32 pixels by 32 pixels. The camera equipped with AF Nikkor 35-105 mm lens and a Nikon No. 1 Close-Up **lenscan** be seen at the bottom center in Fig. 1(a). The image resolution in the present experiments varied from 128 pixels \times 224 pixels to 196 pixels \times 400 pixels, depending on chamber pressure and outer-to-inner momentum flux ratio. The images were in a grayscale scale with each pixel taking a value between 0 and 255 for different intensities of gray ranging from white to black. Each pixel represents an approximate area of 0.08 mm \times 0.08 mm. Depending on the resolution chosen, the framing rate was 20, 25 or 41 kHz. The exposure time was generally 1-2 μ s and the number of images saved per run

was 1000.

The images recorded were then processed using a Matlab subroutine based on the Otsu technique [44]. The subroutine takes a grayscale image and finds a pixel threshold value. All the pixel values above this threshold are converted to black and the remaining pixels to white. Then the subroutine measures the length of the black region extending from the exit of the coaxial jet. This is referred to as the “dark core length”. A “mean dark core length” l_{dc} is then obtained by averaging over the set of images recorded by the camera. Acoustic modulation of this setup was obtained with two piezo-sirens placed at each end of the chamber at a distance of 34 cm from the jet axis, custom-designed for the Air Force Research Laboratory by Hersh Acoustical Engineering, Inc (the piezo-sirens can be seen at both sides of the chamber in Fig. 1(a)). A Fluke 100 MS/s arbitrary waveform generator (model 292) was used to produce two sinusoidal waves with the same frequency but with a prescribed phase between them. The signals were then sent to two amplifiers (Krohn-Hite model 7500 and a Trek model PZD2000A), one for each piezo-siren. The amplified signals were in the 200 to 540 V range. To accommodate for the rectangular chamber, a waveguide with a catenary contour - see upper left corner of Fig. 1(a) - was used to transmit the waves from the circular cross-section of each siren to a rectangular cross-section. The maximum root-mean-square acoustic pressure fluctuations generated by the two piezo-ceramic acoustic sources in the inner chamber, measured using the three differential Kulite pressure transducers (model XCQ-093-25D) flush mounted on a lateral chamber wall, varied from 8.0 to 22 kPa and were produced in the 2.9 to 3.1 kHz range. These operating conditions were obtained by manually varying the frequency on the signal generator and finding the highest possible pressure amplitude.

The phase difference between the signals sent to the piezo-siren elements was varied to expose the coaxial jet to different effective positions relative to the pressure node or antinode of the acoustic field. When the two piezo-siren elements produce waves with a zero degree phase angle between them, the motion of the piezo-siren radiating membranes is synchronized and radiates in opposite directions. This produces conditions of high

pressure perturbations and low velocity fluctuations at the center of the chamber, where the coaxial jet is located, which correspond to a pressure antinode or velocity node. In contrast, when the two drivers present a 180-degree phase difference, then the radiating membranes move in the same direction, generating high velocity fluctuations with very small variations in pressure at the jet location, producing a pressure node or velocity antinode.

3 Balance equations and models

At this stage it is worth briefly reviewing the spatially filtered balance equations and introducing the real gas models and subgrid scale closures used in the large eddy simulations.

3.1 Governing equations

A single species flow configuration is investigated in the present study. In this situation, the vector of conservative variables for a compressible flow is $\mathbf{w} = (\rho, \rho\mathbf{u}, \rho E)^T$, where ρ is the density, \mathbf{u} the velocity vector and E the total energy (E is the sum of internal energy e_s and kinetic energy $e_k = 1/2 \sum u_i^2$). The present large-eddy simulations are carried out by integrating the mass weighted spatially filtered Navier-Stokes equations. In the following balance equations (for a given variable ϕ , $\bar{\phi}$ designates the spatially filtered variable, while $\tilde{\phi}$ is the mass-weighted (Favre) spatially filtered variable) :

$$\frac{\partial \bar{\rho}}{\partial t} + \frac{\partial \bar{\rho} \tilde{u}_j}{\partial x_j} = 0 \quad (1)$$

$$\frac{\partial \bar{\rho} \tilde{u}_i}{\partial t} + \frac{\partial \bar{\rho} \tilde{u}_j \tilde{u}_i}{\partial x_j} = -\frac{\partial \bar{p}}{\partial x_i} + \frac{\partial \bar{\tau}_{ij}}{\partial x_j} - \frac{\partial \tau_{ij}^t}{\partial x_j} \quad (2)$$

$$\frac{\partial \bar{\rho} \tilde{E}}{\partial t} + \frac{\partial \bar{\rho} \tilde{E} \tilde{u}_j}{\partial x_j} + \frac{\partial \bar{p} \tilde{u}_j}{\partial x_j} = -\frac{\partial \bar{q}_j}{\partial x_j} - \frac{\partial q_j^t}{\partial x_j} + \frac{\partial \tilde{u}_i \bar{\tau}_{ij}}{\partial x_j} \quad (3)$$

In Eqs. 1-3, p is the pressure, \boldsymbol{x} the spatial coordinates vector and t is the time. The laminar viscous stress tensor $\boldsymbol{\tau}$ and heat flux vector \boldsymbol{q} are expressed as linear functions of the strain rates and temperature gradient respectively. Laminar viscosity and heat conductivity coefficients are determined with the Chung *et al.* method [12]. For the single species case investigated in the present article, no additional diffusion terms are needed since the Soret and Dufour effects naturally vanish. The modeling of the subgrid-scale stress tensor τ_{ij}^t and heat flux vector q_j^t requires some discussion. It is known from recent studies that subgrid closure rules for real gases differ from those used for perfect gas flows. In principle one should take into account additional terms arising from the nonlinearity of the state equation, and from the large variations in transport properties as explained in some recent studies by Bellan *et al.* [2], Selle *et al.* [63] and Taskinoglu and Bellan [68]. However the modeling issues are not completely settled. It is also known from other calculations that the low pressure subgrid scale models yield suitable results for transcritical and supercritical round jets [59, 62]. It was decided for these reasons to keep these low pressure closures for the subgrid scale models as described in more detail in Sec. 3.3.

3.2 Real gas thermodynamics and equation of state

Real gas thermodynamics for high pressure flow calculations is envisaged in many recent studies where accurate descriptions of the fluid state are derived from various types of equations [1, 71]. The present simulations rely on the Peng-Robinson equation of state [45] (Eq. 4) which is used in the analysis to model the departure from an ideal-gas behavior. This EOS is less accurate than the modified version but it is also simpler and requires a smaller amount of calculations. The fluid state is expressed in the form :

$$p = \frac{\rho r T}{1 - \rho b} - \frac{\rho^2 a(T)}{1 + 2\rho b - \rho^2 b^2} \quad (4)$$

where T is the temperature, $r = R/W$ where R is the perfect-gas constant and W the molar mass. The Peng-Robinson coefficients $a(T)$ and b for a single-species fluid are [47]:

$$a = 0.457236 \frac{(rT_c)^2}{p_c} \left(1 + c(1 - \sqrt{T_R})\right)^2 \quad (5)$$

$$b = 0.077796 \frac{rT_c}{p_c} \quad (6)$$

with

$$c = 0.37464 + 1.54226\omega - 0.26992\omega^2 \quad (7)$$

where $T_c = 126.2$ K and $p_c = 3.396$ MPa are the critical temperature and pressure of nitrogen, $\omega = 0.0372$ represents its acentric factor and $T_R = T/T_c$ is the reduced temperature. This equation offers a good trade-off between computational cost and precision. The pressure dependence of thermodynamic functions and coefficients is subsequently derived from the EOS [33, 38, 71]. Departure energy Δe_s and specific heat Δc_v at constant volume are given by [20, 47]:

$$\Delta e_s = - \int_{\rho}^{\rho_0} \left\{ \frac{T}{\rho^2} \left(\frac{\partial p}{\partial T} \right)_{\rho, Y_k} - \frac{p}{\rho^2} \right\}_T d\rho \quad (8)$$

$$\Delta c_v = -T \int_{\rho}^{\rho_0} \left\{ \left(\frac{1}{\rho^2} \frac{\partial^2 p}{\partial T^2} \right)_{\rho, Y_k} \right\}_T d\rho \quad (9)$$

where $\Delta e_s = e_s(\rho, T) - e_s^0(T)$ and $\Delta c_v = c_v(\rho, T) - c_v^0(T)$. The enthalpy and specific heat at constant pressure are then deduced from :

$$h_s = e_s + \frac{p}{\rho} \quad c_p = c_v + \frac{T\alpha^2}{\rho\beta} \quad (10)$$

The thermal expansion coefficient α and the isothermal compressibility coefficient β appearing in the previous expressions are given by:

$$\alpha = -\frac{1}{\rho} \left(\frac{\partial \rho}{\partial T} \right)_p \quad \beta = \frac{1}{\rho} \left(\frac{\partial \rho}{\partial p} \right)_T \quad (11)$$

The low-pressure references (*i.e.* e_s^0 and c_v^0) are obtained from the JANAF Thermodynamical Tables [7], and only depend on temperature.

3.3 Subgrid-scale models and assumptions

As indicated previously, the present simulations rely on a standard (low pressure) subgrid scale closure, the WALE model, in which the stress tensor τ_{ij}^t is conveniently expressed in terms of the spatially resolved strain rates \tilde{S}_{ij} [35] :

$$\tau_{ij}^t = 2\nu^t \left(\tilde{S}_{ij} - \frac{1}{3} \delta_{ij} \tilde{S}_{ll} \right) \quad (12)$$

where

$$\nu^t = (C_w \Delta)^2 \frac{(s_{ij}^d s_{ij}^d)^{3/2}}{(\tilde{S}_{ij} \tilde{S}_{ij})^{5/2} + (s_{ij}^d s_{ij}^d)^{5/4}} \quad (13)$$

$$s_{ij}^d = \frac{1}{2} (\tilde{g}_{ij}^2 + \tilde{g}_{ji}^2) - \frac{1}{3} \tilde{g}_{kk}^2 \delta_{ij} \quad (14)$$

In the previous expression the WALE model constant $C_w = 0.4929$ and \tilde{g}_{ij} is the irrotational part of the stress tensor :

$$\tilde{g}_{ij} = \frac{\partial \tilde{u}_i}{\partial x_j} \quad \text{and} \quad \tilde{g}_{ij}^2 = \tilde{g}_{ik} \tilde{g}_{kj} \quad (15)$$

The WALE model distinguishes velocity gradients associated with the rotational and pure shear components of the velocity gradients in order to distinguish regions where turbulence is transitional and regions where it is fully developed. It is well suited to the treatment of shear flows of the type considered in this article.

The subgrid scale heat flux is modeled using a standard gradient transport assumption :

$$\overline{q}_i^t = -\lambda_t \frac{\partial \tilde{T}}{\partial x_i} \quad (16)$$

The subgrid scale conductivity is cast in the form $\lambda_t = c_p \mu_t / \text{Pr}_t$ where $\mu_t = \rho \nu_t$ and Pr_t respectively designate the subgrid dynamic viscosity and turbulent Prandtl number. As in low pressure simulations a constant value $\text{Pr}_t = 0.7$ is used in the present calculations.

4 Numerical aspects

The mass weighted spatially filtered compressible Navier-Stokes equations in combination with the subgrid scale models described previously are integrated in the AVBP flow solver [60, 34]. This code has already been used to calculate low and moderate pressure reactive flows of multicomponent mixtures of perfect gases. The spatial discretization on unstructured or hybrid meshes facilitates applications in which the geometry is complex, a feature which is quite useful if one wishes to analyze practical configurations. The LES of turbulent flows requires a low-dissipation algorithm [21, 18] which is often obtained with centered discretization schemes. The present integration method relies on a Taylor-Galerkin weighted residual central distribution scheme, called TTG4A. This scheme is third-order in space and fourth-order in time [50].

The real gas equation of state, thermodynamics and transport coefficients have been implemented in AVBP. The convective fluxes Jacobian matrices, used by the scheme, are expressed in terms of real gas thermodynamics to preserve the overall consistency of the code. A fully consistent treatment of associated boundary conditions is based on the characteristic wave decomposition method NSCBC [46, 34] and includes specific expressions provided for real gas thermodynamics in [39]. The highly nonlinear thermodynamics of the transcritical fluid stream induces large density gradients between the dense transcritical fluid and the surrounding gaseous stream which require a specific stabilization procedure. This relies on artificial viscosity and is used when unresolved gradients are

detected following a method described in [59]. The real gas AVBP flow solver has already been used to simulate transcritical cryogenic flames of various types [48, 58, 57].

4.1 Computational domain and mesh

The geometry of the computational domain essentially matches the experimental configuration. A three-dimensional view of the external boundaries is given in Fig. 3(a). The longitudinal section of the chamber is rectangular (59.4×76.0 mm) and its width is 12.7 mm. The fluid streams are injected by a coaxial element which protrudes by 5 mm into the chamber (Fig. 3b). This injector is located in the center of a 17 mm-diameter hole in the inlet wall. No co-flow is directly injected through this orifice during the experiment, but nitrogen gas may traverse this aperture as a result of entrainment by the coaxial streams giving rise to a finite flow velocity in this region. The entrained fluid originates from a large reservoir defined on the upstream side of the central hole. Details about the injector geometry are given in Fig. 4(a). The inner injector diameter, inner duct thickness, annular duct thickness and outer duct diameter are respectively $d_i = 0.51$ mm, $l_i = 0.54$ mm, $h_e = 0.415$ mm and $d_o = 2.42$ mm. The mesh comprises 2 100 000 nodes

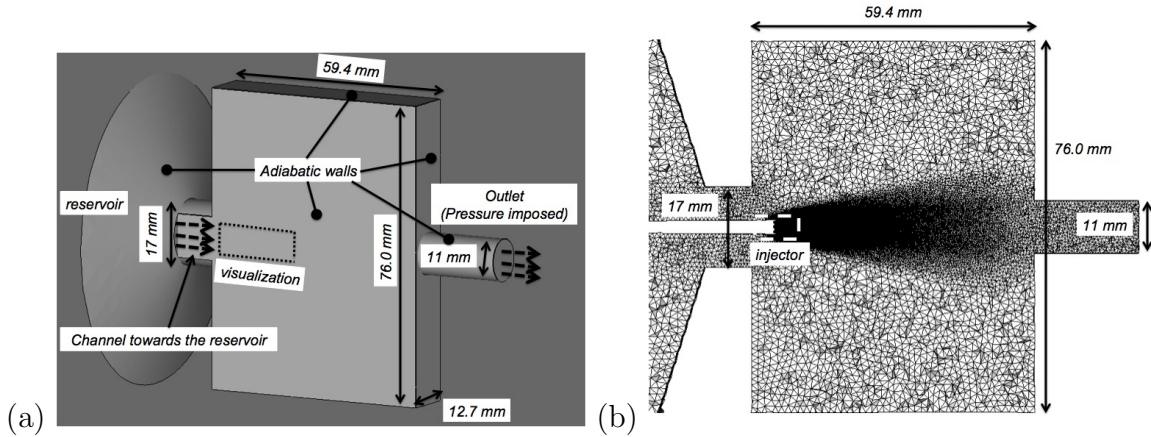


Figure 3: (a) Three-dimensional visualization of the reservoir. (b) Longitudinal cut of the mesh.

corresponding to 10 000 000 tetrahedra. It is highly refined near the injector (Fig. 4(b)), with a constant characteristic size of 0.032 mm on a distance of 10 inner jet diameters.

The mesh is then slowly coarsened towards the domain outlet (Fig. 3(b)).

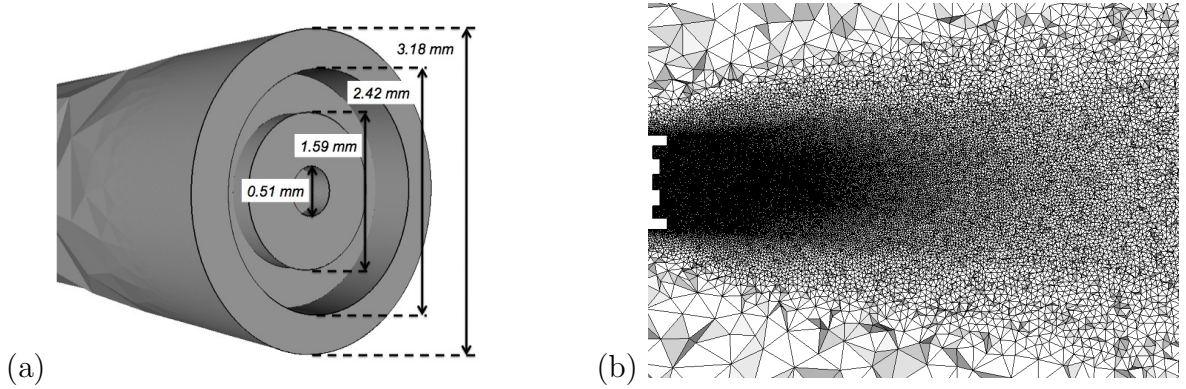


Figure 4: (a) Closer view of the injector. (b) Longitudinal cut of the mesh (35 inner injector diameters).

4.2 Injection characteristics and boundary conditions

Three test conditions are considered in this analysis designated as “N2”, “N6” and “N8”. Case “N6” serves as a reference simulation. The two other cases, designated as “N2” and “N8”, are also calculated in order to analyze effects of the momentum flux ratio on the flow behavior (Sec. 5). The three cases differ by their injection temperatures and velocities, yielding momentum flux ratios J of 1, 2.6 and 9.1 for cases “N2”, “N6” and “N8” respectively. The corresponding density ratios S are 5.84, 5.74 and 3.22 respectively. Injection conditions are gathered in Tab. 12 and Tab. 13 which respectively correspond to the outer and inner streams. Injection conditions are placed on thermodynamic plots on Fig. 5. The density and volumetric internal energy notably depart from a perfect gas behavior when temperature is close and below the critical value. The influence of acoustic perturbations will only be investigated in a single case corresponding to “N6” (Sec. 6).

In all cases, pressure is maintained at the outlet boundary using non-reflecting characteristic conditions at an adapted level of 3.56 MPa, and the chamber and reservoir are initially filled with nitrogen at the same pressure and a temperature 213 K (the corresponding density is 59.6 kg m^{-3}). All solid boundaries are treated as adiabatic slip walls. Velocity perturbations (with an amplitude of 3 % of the mean flow) are added at injec-

tion in order to represent effects of turbulent fluctuations using a procedure described in [6, 66, 17].

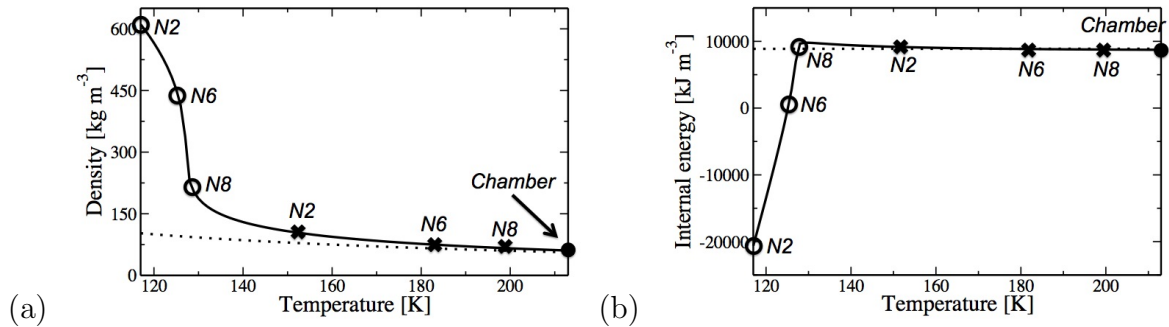


Figure 5: Thermodynamic state calculated with the PR EOS (—) and the perfect gas EOS (· · ·). (a) Density in terms of temperature. (b) Volumetric internal energy (*i.e.* ρe_s) in terms of temperature. The pressure is constant and equal to 3.56 MPa. Symbols: ○ inner jet conditions; × outer stream conditions; ● chamber conditions.

Case	$J = (\rho_e u_e^2)/(\rho_i u_i^2)$	$M = (\rho_e u_e)/(\rho_i u_i)$	$S = \rho_i/\rho_e$	$U = u_e/u_i$
N2	1.05	0.42	5.86	2.48
N6	3.05	0.72	5.65	4.15
N8	9.3	1.70	3.22	5.48

Table 1: Injection characteristics of the simulated cases. J is the momentum flux ratio between the outer and the inner jets, M the mass flux ratio, S the density ratio and U is the velocity ratio. ρ_i , ρ_e , u_i and u_e are the inner and outer jet densities and velocities.

4.3 Simulation procedure

Simulations are carried out on a coarse mesh, with an initial solution corresponding to a uniform fluid at rest. The flow is then qualitatively established after three convective periods. Results are then interpolated on the final mesh. Data averaging can be started after one transient period. The simulated physical time is given in Tab. 2 together with the number of simulated convective periods. Finally, the CPU time (equal to the product $n_{core} \times n_{hours}$) needed to obtain the average solution (which does not include the CPU time needed for the transient flow and the simulation on the coarse mesh) is also given in this table.

Case	Δt^a [ms]	$\Delta t^a/\tau_{u_i}$	$\Delta t^a/\tau_{u_e}$	CPU time [h]
N2	14.3	1.9	4.8	35 000
N6	22.7	4.4	18.2	45 000
N8	10.4	4.0	21.2	20 000

Table 2: Averaging time for cases “N2”, “N6” and “N8”. Δt^a is the physical averaging time. τ_{u_i} represents one convective time over $35 d_i$ for the inner jet and τ_{u_e} represents one convective time over $35 d_i$ for the outer jet. $\tau_{u_i} = (35d_i)/u_i$; $\tau_{u_e} = (35d_i)/u_e$.

5 Effect of momentum flux ratio

It is first natural to consider the influence of the momentum flux ratio on the system behavior. Flow patterns calculated numerically and obtained experimentally are first compared in Sec. 5.1. This is followed by a description of the mean flow in Sec. 5.2 and by an analysis of flow dynamics in Sec. 5.3.

5.1 Instantaneous flow patterns

Instantaneous backlighting images obtained experimentally are shown in Fig. 6(a),(c),(e). In the dark core light is deviated by changes in the refraction index. This in turn delineates regions where the density takes large values (the deviation can be roughly linked to the second derivative of the density integrated on the line of sight). It is generally admitted that the dark region represents the position of the dense core, and qualitatively highlights its external boundaries giving an insight on the main structures present in the flow [43]. As the momentum flux ratio is increased, the inner jet axial length is reduced. Case “N2” exhibits large scale structures over about 10 inner injector diameters downstream of the injector. These structures are not identifiable in cases “N6” and “N8”. The latter is characterized by a sudden termination of the inner jet at a few inner jet diameters from the exit plane. In contrast with cases “N2” and “N6”, the inner stream appears to be quickly mixed with the surrounding fluid, and the central jet can no longer be clearly identified downstream of this abrupt termination.

Longitudinal slices of instantaneous density distributions extracted from simulations are

shown in Fig. 6(b),(d),(f) which respectively correspond to “N2”, “N6” and “N8” cases. Comparisons between these figures and the experimental backlighting images are admittedly qualitative. Nevertheless, general experimental features corresponding to these different cases are replicated. One finds that case “N2” features large scale structures which are not present in cases “N6” and “N8”. The abrupt termination noticed in case “N8” is retrieved numerically. This is also made more apparent in the density iso-surfaces corresponding to $\rho = 0.1(\rho_i - \rho_e) + \rho_e$ plotted in Fig. 7. The large scale structures observed experimentally characterize case “N2”, and disappear as the momentum flux ratio is increased (cases “N6” and “N8”).

5.2 Mean flow description

It is first interesting to examine effects of the momentum flux ratio on the mean “dark core” length. Since the density field cannot be directly compared to the experimental light distribution images, it is natural to define a set of density length scales and compare them with the dark core length deduced from the data. The jet core characteristic lengths are defined by considering the axial density distribution :

$$l_\rho^{0.99} = x_\rho^{0.99} - x_0 \quad l_\rho^{0.5} = x_\rho^{0.5} - x_0 \quad l_\rho^{0.1} = x_\rho^{0.1} - x_0 \quad (17)$$

where x_0 is the axial position of the inner injector exit, $x_\rho^{0.99}$, $x_\rho^{0.5}$ and $x_\rho^{0.1}$ are positions on the jet axis where density is respectively equal to 99 % of its initial value, to $0.5(\rho_i - \rho_e) + \rho_e$ or to $0.1(\rho_i - \rho_e) + \rho_e$. These three lengths are shown in Fig. 8(a) together with mean density profiles on the centerline.

It is also useful to define at this point another length scale based on the axial mean velocity profile. The central jets all feature an initial decrease in the axial velocity on the centerline as can be seen in Fig. 8(b). The minimum value is reached at x_u which is used to define a new length scale $l_u = x_u - x_0$.

Characteristic lengths are gathered in Tab. 3 for comparison with experimental mea-

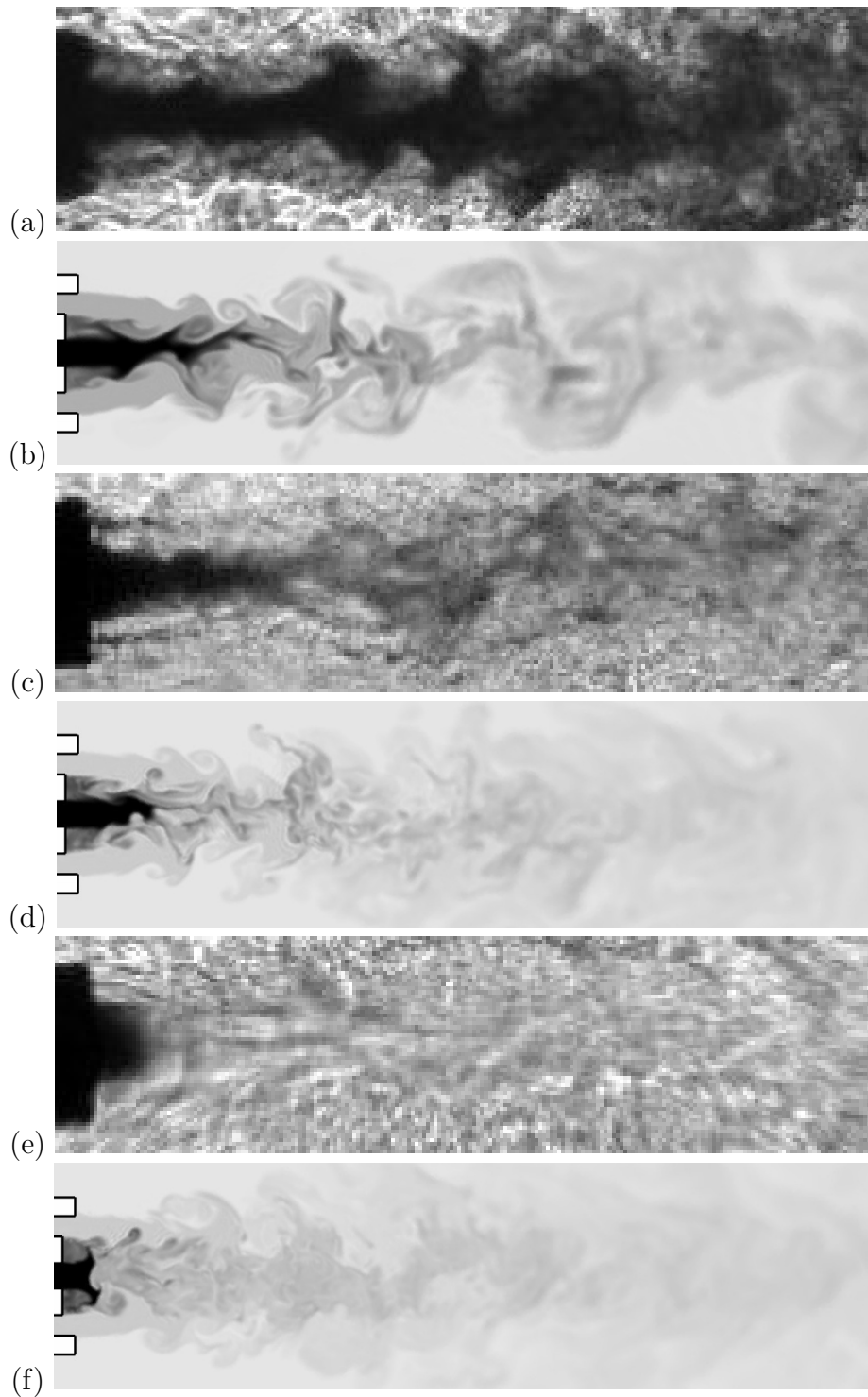


Figure 6: Comparison between experimental visualizations (backlighting) and typical instantaneous density distributions obtained from simulations (white: 60 kg m^{-3} ; black: inner jet injection density (Tab. 13) ; logarithmic scale). Case “N2” ($J=1.05$) : (a) Experimental backlighting image, (b) Calculated density. Case “N6” ($J=3.05$) : (c) Experimental backlighting image, (d) Calculated density. Case “N8” ($J=9.3$) : (e) Experimental backlighting image, (f) Calculated density.

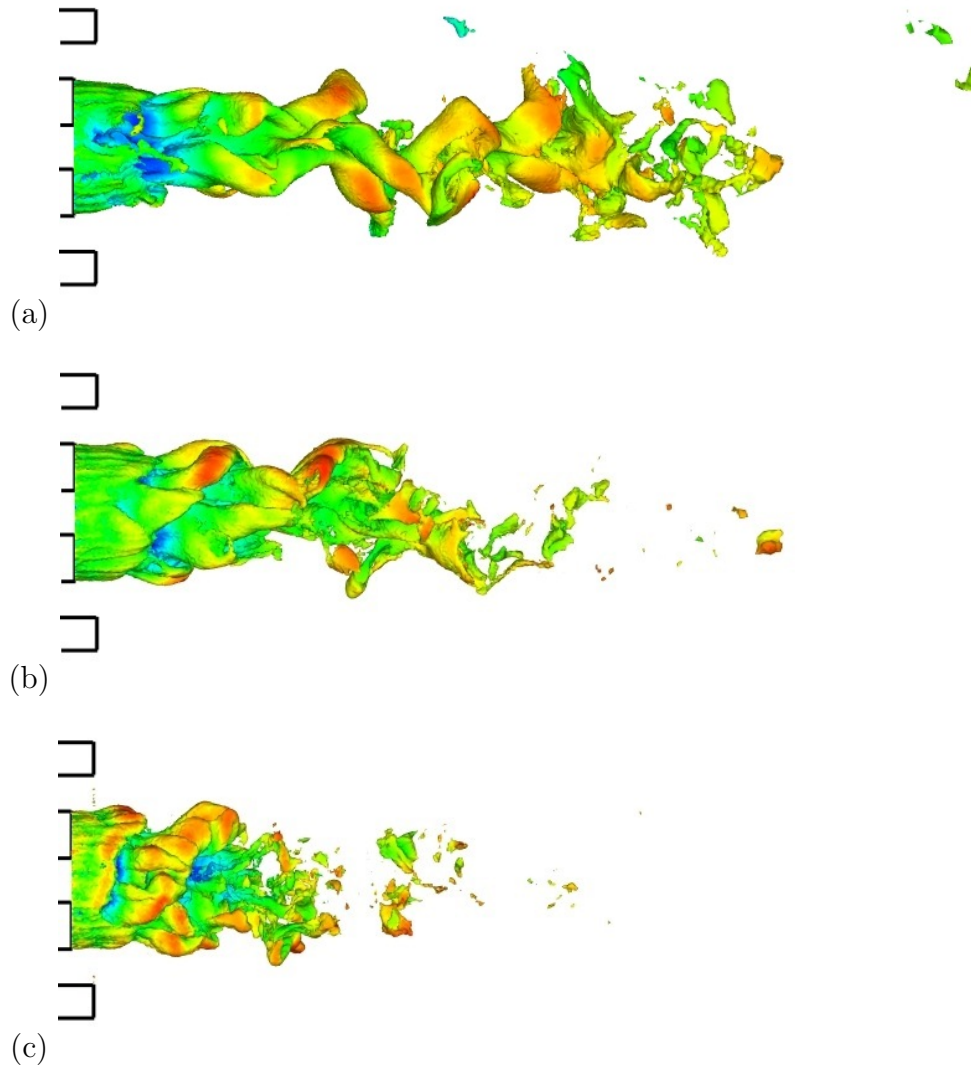


Figure 7: *LES results*. Density iso-surface corresponding to $\rho = 0.1(\rho_i - \rho_e) + \rho_e$ colored by the axial velocity. (a) case “N2” ($J=1.05$) $u_{min}=-2$ m s⁻², $u_{max}=6.5$ m s⁻², (b) case “N6” ($J=3.05$) $u_{min}=-4$ m s⁻², $u_{max}=16$ m s⁻², (c) case “N8” ($J=9.3$) $u_{min}=-5$ m s⁻², $u_{max}=40$ m s⁻². The plot corresponds to 20 inner injector diameters.

measurements of the “dark core” length. The latter values are deduced from backlighting images by measuring the “dark region” size from average images. Again, comparison between experiment and simulation is limited. As already noted in [43], lengths deduced from experimental backlighting data are generally larger than those deduced from density measurements. It is however clear that there are similarities between trends in simulations and experiments. In agreement with experiments, numerical results indicate a reduction in the density length scales as the momentum flux ratio is increased. The velocity length scale is reduced and the amplitude of the velocity defect is enhanced as the momentum flux ratio is increased. The flow may also be characterized by the distributions of mean

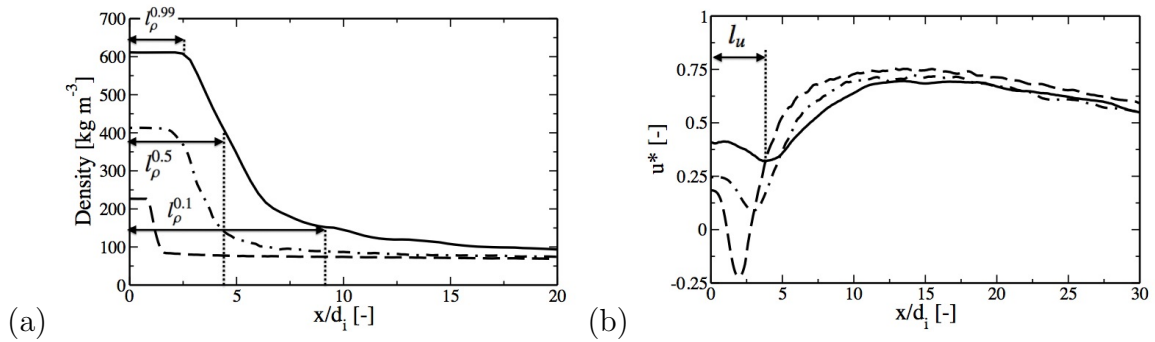


Figure 8: Centerline profiles deduced by averaging LES results. (a) Density, (b) Axial velocity normalized by the outer injection velocity $u^* = u/u_e$. — : Case “N2”, - · - : Case “N6” and - - : Case “N8”.

Case	$l_{\rho}^{0.99}/d_i$	$l_{\rho}^{0.5}/d_i$	$l_{\rho}^{0.1}/d_i$	l_u/d_i	l_{dc}/d_i
N2	2.57	4.40	8.66	3.8	15.5
N6	1.81	3.37	5.88	2.95	6.0
N8	0.85	1.17	1.67	1.96	2.5

Table 3: Characteristic lengths deduced from simulations based on axial density and velocity profiles and from experimental measurement of the dark core size.

axial velocity plotted in Fig. 9. The outer flow contracts towards the central stream and pinches the central jet to a point where this stream disappears. In the three cases, a small back-flow is generated behind the injector lips. As the momentum flux ratio is increased beyond a certain critical value (case “N8”), the central jet is surrounded by a negative axial velocity region (Fig. 9c).

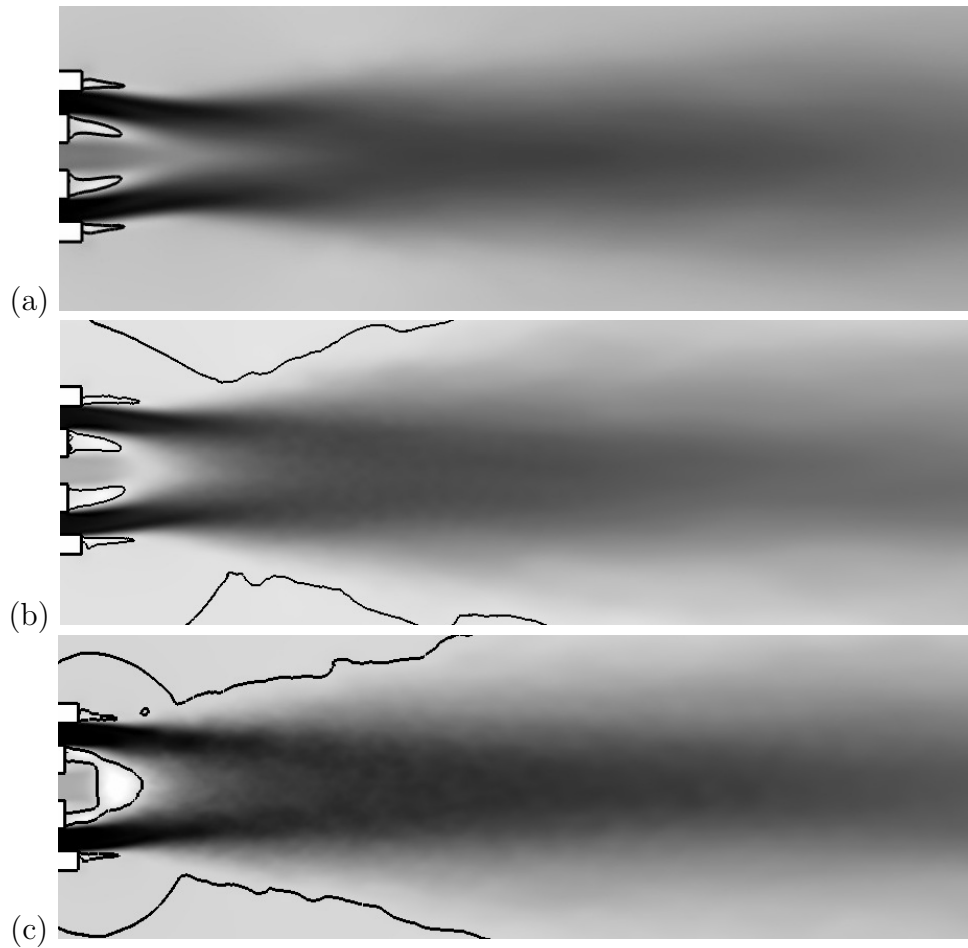


Figure 9: Distribution of axial velocity (white: minimum ; black: maximum). This map corresponds to 35 inner injector diameters. — iso-contour of zero axial velocity. (a) case “N2” ($J=1.05$), (b) case “N6” ($J=3.05$), (c) case “N8” ($J=9.3$).

Case “N8” exhibits a large negative value, as observed previously in Fig. 9(c). Further downstream, the flows behave in a self-similar fashion in terms of axial velocity normalized by the outer jet injection velocity. Beyond this section, the impact of the inner jet on the flow disappears as this jet is mixed with the outer stream. Since the mass flow rate of the outer jet is much higher than that of the inner jet, the outer jet dominates the flow. Interestingly, the three profiles merge at $x > 15d_i$, indicating a self-similar behavior when profiles are plotted in terms of normalized variables.

Radial profiles of normalized density and axial velocity are plotted in Fig. 10 for case “N6” (case “N2” is not shown here because its behavior is quite similar). The first profiles lie in the potential core region ($x < x_\rho^{0.99}$), and feature constant levels of density and velocity in that region. Negative values of axial velocity indicate that back-flow is generated behind the lips. The density profile behind the inner lip shows a rapid variation towards the outer stream. This is attributed to an efficient mixing of inner and outer streams associated with the formation of vortical structure behind the inner lip and the generation of a back flow. In this region, mass is extracted from the central jet by vortical structures and recirculates upstream. Dynamics in this region are discussed in Sec. 5.3. The profile at $3d_i$ corresponds to $x = x_u$. The density stratification is still apparent. At $x = 15d_i$, velocity and density are maximum on the centerline, and a jet-like profile is retrieved. Further downstream, the flow behaves like a single round jet and develops in a self-similar fashion. The half width at half maximum (HWHM) of density L_ρ is plotted in Fig. 11(a). For $x > 20d_i$, this quantity evolves quasi-linearly $L_\rho = E_\rho^H(x - x_v)$, where E_ρ^H is the spreading rate of the jet and x_v is a virtual origin. Linear regressions for $20d_i < x < 35d_i$ give spreading rates of 0.12, 0.11 and 0.11 for cases “N2”, “N6” and “N8”, respectively. These values are in agreement with those given for example by Chen and Rodi [10] for a single jet and with results obtained from previous high pressure simulations of single species round jets [59, 76]. In this region of the flow, the density profile takes a gaussian shape (Fig. 11b). A linear evolution of the density decay is also observed, but not shown here, confirming that the flow is self-similar in the downstream region. Since

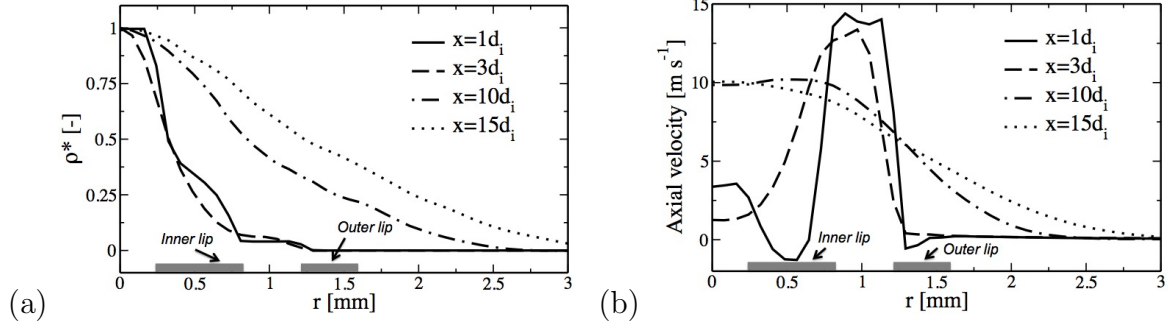


Figure 10: *LES results*, Case “N6”. (a) Radial profiles of normalized density $\rho^* = (\rho - \rho_\infty)/(\rho_c - \rho_\infty)$ (b) Radial profiles of axial velocity.

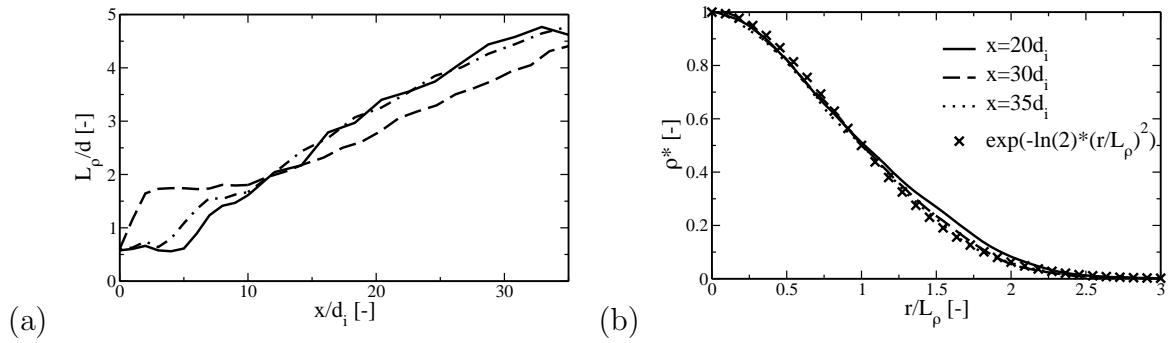


Figure 11: *LES results* (a) Half Width Half Max of density — Case “N2”, — · — Case “N6” and — — Case “N8”. (b) Radial profiles of normalized density $\rho' = (\rho - \rho_\infty)/(\rho_c - \rho_\infty)$.

the flow develops in a confined domain, one may wonder if it is influenced by recirculation in the chamber. Examination of velocity distributions in the domain indicates that the outer recirculation velocities are low and that the reverse flow in the outer region has a limited influence on the coaxial jet structure.

5.3 Near injector flow dynamics

Large eddy simulations allow detailed analysis of the flow dynamics. This can be accomplished by estimating the spectral content of fluctuations in various regions of the flow to identify the preferred modes of the system. To this end, it is convenient to place a set of sensors in the flow and examine the corresponding velocity and density time series. This is illustrated in Fig. 12. Since the general flow structures of cases “N2” and “N6” differ from that corresponding to “N8”, it is natural to study these two cases separately (Sec. 5.3.1). Case “N8” is then considered in Sec. 5.3.2.

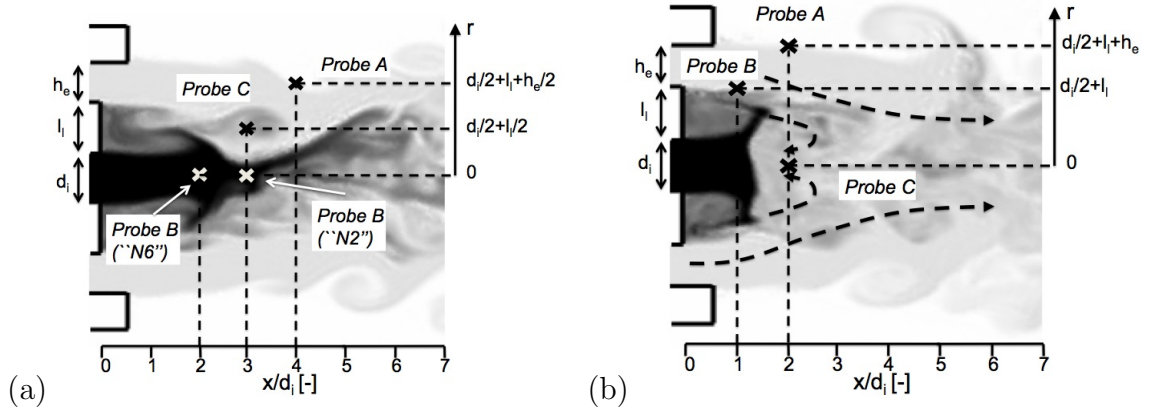


Figure 12: The three sensor locations. The numerical probes are used to measure characteristic frequencies in the coaxial flow. (a) Case “N6” ($J=3.05$). Density distribution (white: 60 kg m^{-3} ; black: 410 kg m^{-3} ; logarithmic scale). Sensor B is placed at the end of the inner jet potential core which corresponds to different location in cases “N2” and “N6”. (b) Case “N8” ($J = 9.3$). Density distribution (white: 60 kg m^{-3} ; black: maximum ; logarithmic scale). Sensor C is located in the recirculation region.

5.3.1 Cases “N2” and “N6”

To examine the spectral information it is natural to define a set of Strouhal numbers associated with characteristic scales and velocities in the region of interest. The meaningful length scales in this study are the inner injector diameter d_i , the inner lip thickness l_l and the annular jet thickness h_e . Two velocities characterize the system : the inner and outer jet injection velocities (u_i and u_e , respectively). The resulting Strouhal numbers and the probes used to measure frequencies are shown in Tab. 4. Probes A and B are used to evaluate the fundamental frequencies of the outer and inner streams. Probe C provides the dominant frequency associated with eddy structures released behind the injector lip and associated with the outer jet. From instantaneous snapshots (see Fig. 12 for example) and animations, these structures are found to originate from the lip corner on the outer-jet side. Positions of the different probes are shown in Fig. 12 (a). Note that the axial location of probe B is not the same in cases “N2” and “N6”, because this probe is placed at the end of the potential core. Power spectral densities are estimated using Welch’s method of periodograms. Statistical averaging is obtained by segmenting the finite data set in M overlapping blocks (a 50 % overlap is used to augment the number of periodograms used in the averaging procedure). Because the number of samples is limited, the averaging is carried out over $M = 8$ blocks in the outer flow and on $M = 4$ blocks in the inner jet (power is concentrated in the low frequency range and it is important to augment the resolution to distinguish the maximum frequency). The frequency resolution corresponding to the different sensors is given in Tab. 4.

$St = (fl)/u$	l	u	Probe (Fig. 12(a))	Δf [Hz]
St^e	h_e (0.41 mm)	u_e	A	N2: 375 ; N6: 250
St^i	d_i (0.51 mm)	u_i	B	N2: 187 ; N6: 125
St^l	l_l (0.54 mm)	u_e	C	N2: 375 ; N6: 250

Table 4: Definition of characteristic Strouhal numbers. The characteristic length and velocity l and u are given in the second and third columns. The frequency f corresponds to the power spectral density maximum estimated from the simulations. Δf is the frequency resolution.

The outer and central streams are destabilized at a few diameters d_i from the injector exit. The measured frequency for the outer jet (probe A) is 3 600 Hz for case “N2” and 8 550 Hz for case “N6” (Fig. 13), which correspond to $St_{N2}^e=0.25$ and $St_{N6}^e=0.25$. The central high-density jet presents a fundamental instability at 1 620 Hz and 1 740 Hz for cases “N2” and “N6” (Fig. 14) respectively (probe B). The associated Strouhal numbers are then $St_{N2}^i=0.34$ and $St_{N6}^i=0.26$. For both cases, the fundamental mode of the inner and outer streams falls in the typical range for round jets (0.2 - 0.4).

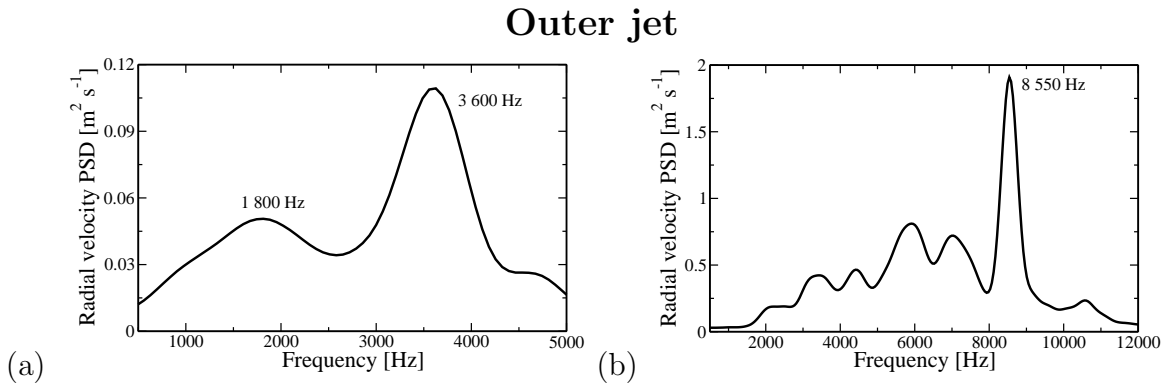


Figure 13: Power spectral density of the radial velocity in the outer jet (probe A). Averaging is carried out on $M = 8$ blocks with a 50% overlap. (a) Cases “N2” ($J=1.05$), (b) Case “N6” ($J=3.05$).

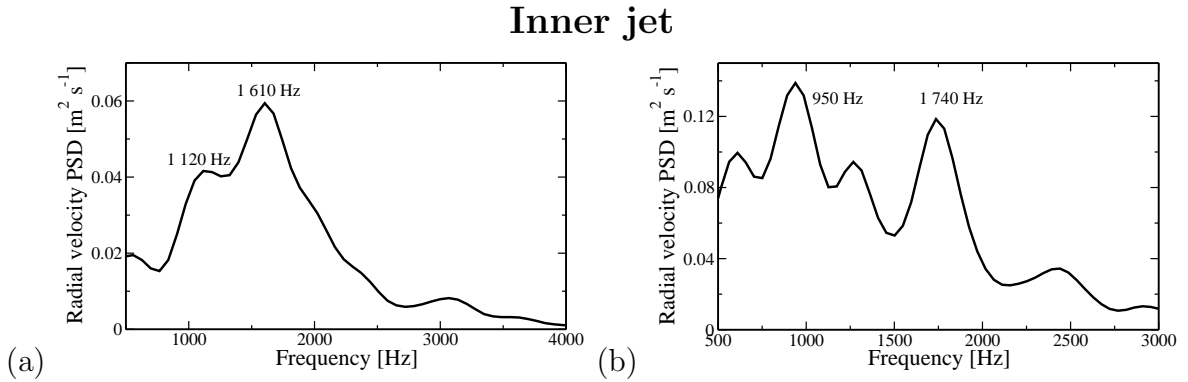


Figure 14: Power spectral density of radial velocity in the inner jet (probe B). Averaging is carried out on $M = 4$ blocks with a 50% overlap. (a) Cases “N2” ($J=1.05$), (b) Case “N6” ($J=3.05$).

The mixing layer between the two jets features eddy structures generated downstream

of the central lip. Their dynamics are similar to those observed for vortices shed behind a backward-facing step. The characteristic frequencies are found to be 1 620 Hz and 3600 Hz, for cases “N2” and “N6” (Fig. 15), respectively. Such frequencies correspond to Strouhal numbers $St_{N2}^l=0.15$ and $St_{N6}^l=0.23$ for cases “N2” and “N6,” which are slightly higher than the commonly determined values for backward-facing step instabilities ($St=O(0.1)$ [70]). This could be attributed to a reduction of the “effective” lip thickness as shear is increased. It turns out that the backward-facing step vortical structures induce a back-flow behind the lip (Fig. 9). High density fluid from the central jet is entrained and recirculates behind the lip. One may then consider that this results in a reduced “effective” lip thickness which intervenes in the formation of the vortical structures, thus limiting their spatial development and increasing the instability frequency. All the Strouhal numbers obtained are gathered in Tab. 5. The frequency obtained for case “N2” is interestingly close to that associated with the inner jet preferred mode. This observation may explain why large scale structures are exclusively observed in this case (Fig. 6).

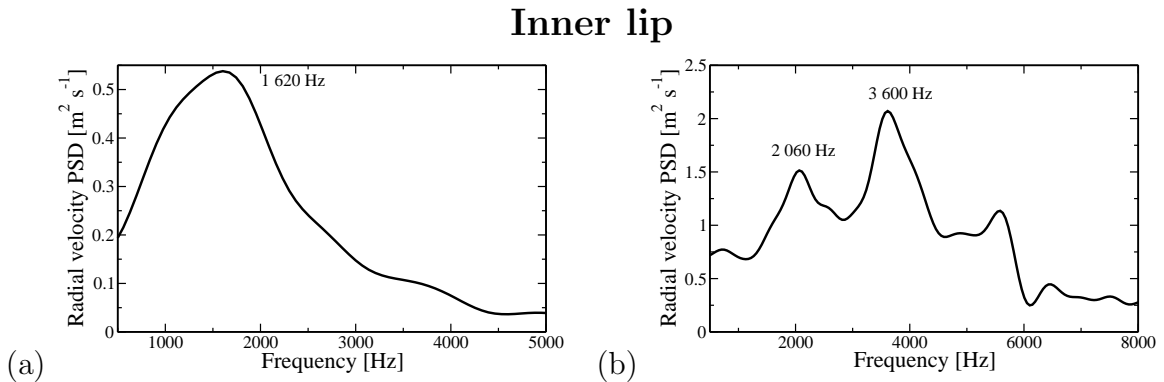


Figure 15: Power spectral density of radial velocity in the mixing layer behind the inner lip (probe C). Averaging is carried out over $M = 8$ blocks with a 50% overlap. (a) Cases “N2” ($J=1.05$), (b) Case “N6” ($J=3.05$).

5.3.2 Case “N8”: recirculation regime

The mechanism leading to mixing of the high density jet with the outer stream is somewhat different for case “N8”. It is already known that the dense jet ends abruptly and

Case	St^e (probe A)	St^i (probe B)	St^l (probe C)
N2	0.25	0.34	0.15
N6	0.25	0.26	0.23

Table 5: Characteristic Strouhal numbers obtained from the simulations for cases “N2” and “N6”.

that a recirculation bubble is established beyond that point. As done previously for cases “N2” and “N6”, characteristic length scales used to define the relevant Strouhal numbers are given in Tab. 6, and the probes used to characterize this case are shown in Fig. 12(b). Probe C is inside the recirculation region and is located at $x = x_u$. This case is highly turbulent and features a broadband spectrum so that temporal data are arranged in $M = 16$ blocks to ensure a reasonable statistical convergence. A 50 % overlap is used to obtain the maximum possible averaging number. The resulting frequency resolution is in this case 1 000 Hz. This value may seem quite high, but should be compared to the spectral range which extends to 25 000 Hz.

$St = (fl)/u$	l	u	probe (Fig. 12(b))
St_{N8}^e	h_e (0.41 mm)	u_e	A
St_{N8}^l	l_l (0.54 mm)	u_e	B
St_{N8}^b	$d_i + l_l$ (0.51+0.54 mm)	u_e	C

Table 6: Strouhal numbers definitions. l and u are the characteristic length and velocity used to define the Strouhal numbers. f represents the frequency obtained from the simulations and Δf is the frequency resolution.

The dominant frequency for the outer jet (probe A) is 21 600 Hz (Fig. 16), which corresponds to $St_{N8}^e=0.25$, as also obtained for the two other cases. The inner jet is notably affected by the recirculation bubble. Its longitudinal development is limited and mass is ejected in the radial direction in the form of thin layers appearing in Fig. 12(b). The resulting structure is similar to a counterflow. This motion leads to the formation of a recirculation ring of high density fluid behind the inner lip with a characteristic size of the order of the lip thickness. Vortex roll-up is observed behind the inner lip, in the mixing layer established between the inner and outer jets. These structures are

similar to those observed in cases “N2” and “N6”, but they strongly interact with higher density layers emerging from the central jet, and their spatial development is limited by the recirculation region. The corresponding Strouhal number is $St_{N8}^l=0.26$ (Fig. 17(a)). These eddy structures lead to the formation of the recirculation region. The measured frequency corresponds to $St_{N8}^b=0.18$ (Fig. 17(b)). The dynamics of this bubble are similar to those observed behind a bluff body terminated by a flat face, for which the characteristic Strouhal number is close to 0.2. The Strouhal numbers obtained in this analysis are gathered in Tab. 7.

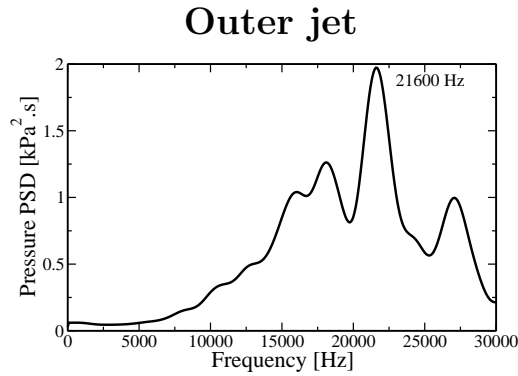


Figure 16: Case “N8” ($J=9.3$). Power spectral density of pressure on Probe A. Averaging is carried out over $M = 16$ blocks with 50% overlap.

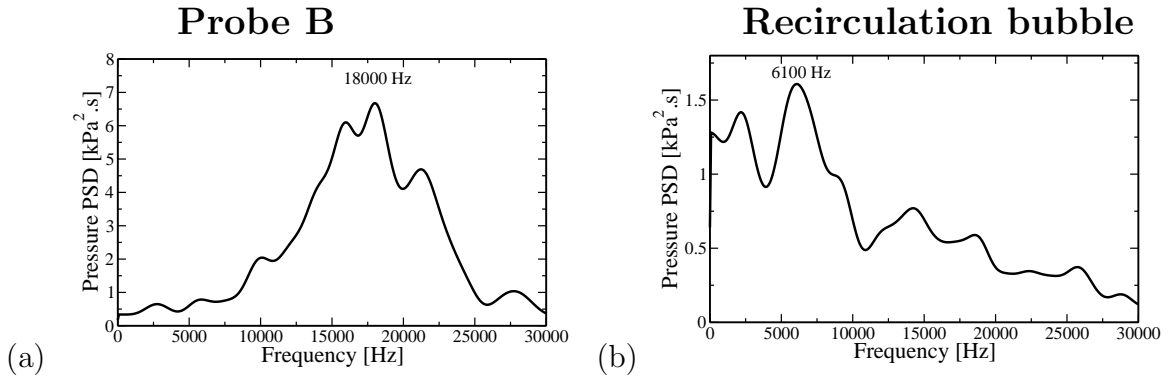


Figure 17: Case “N8” ($J=9.3$). (a) Power spectral density of pressure on Probe B, (b) Power spectral density of pressure in the recirculation bubble. Averaging is carried out over $M = 16$ blocks with 50% overlap.

St_{N8}^e (probe A)	St_{N8}^l (probe B)	St_{N8}^b (probe C)
0.25	0.26	0.18

Table 7: Characteristic Strouhal numbers obtained from the simulations for case “N8”.

6 Effects of a transverse acoustic modulation

Effects of an acoustic modulation are now investigated in case “N6”. This operating point is chosen because the core is sufficiently long to allow an examination of external modulation effects. The methodology used to impose an acoustic excitation is described in Sec. 6.1. Results are then compared with experimental observations in Sec. 6.2 and discussed in Sec. 6.3.

6.1 Modulation methodology

An acoustic modulation is obtained by imposing harmonic modulations of the normal velocity at the outer boundaries using a method devised by Rey *et al.* [52] (Fig. 18). The modulation has the form :

$$v_1 = \sin(2\pi ft) \quad v_2 = \sin(2\pi ft + \phi) \quad (18)$$

where v_1 and v_2 are the normal velocities at the lateral boundaries, f is the modulation frequency set equal to 3 000 Hz, ϕ designates the phase between the imposed modulations. All other boundaries are treated as in the previous cases (in the absence of modulation). This technique is first validated by simulating an acoustic perturbation in the absence of the central flow. Longitudinal distributions of the rms pressure fluctuations are shown in Fig. 19. When $\phi = 0$ (Fig. 19(a)), the normal velocities at the boundaries are in phase, and this yields a maximum pressure fluctuation on the injector axis. A pressure probe placed at 5 mm from the injector exit confirms this behavior. As expected, pressure fluctuations are observed with a 2 % peak-to-peak oscillation with respect to the mean chamber pressure while the transverse velocity remains unperturbed. When the normal

velocities at the boundaries are in phase opposition ($\phi = \pi$), the pressure vanishes on the centerline and the transverse velocity oscillation reaches its maximum (Fig. 19(b)). Spectral analysis also indicates that the perturbed field is dominated by the imposed modulation frequency and that the harmonic content is negligible.

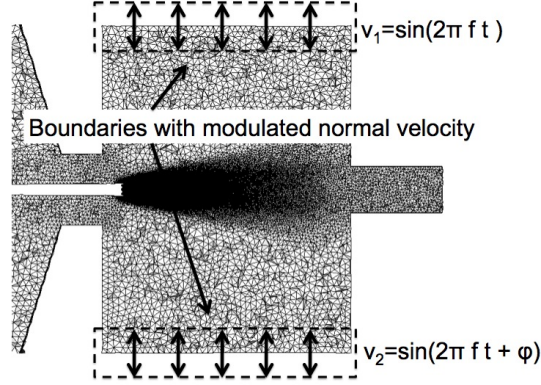


Figure 18: Longitudinal slice in the computational domain showing the methodology retained to impose acoustic perturbation.

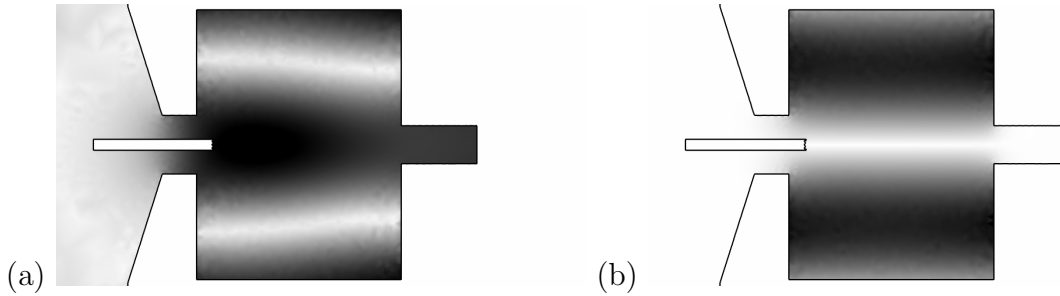


Figure 19: Results obtained under acoustic modulation in the absence of flow. (a) RMS pressure fluctuations for acoustic perturbations in phase ($\phi = 0$). (b) RMS pressure fluctuations for acoustic perturbations in phase opposition ($\phi = \pi$).

The simulated cases are defined in Tab. 8. Injection conditions correspond to case “N6”. Modulation amplitudes of 1 and 2% of the mean chamber pressure are imposed. These two cases are studied for $\phi = 0$ and $\phi = \pi$, respectively, corresponding to a pressure antinode and a pressure node on the central axis.

Case	N6 _{$\phi=0$} ^{2%}	N6 _{$\phi=\pi$} ^{2%}	N6 _{$\phi=0$} ^{1%}	N6 _{$\phi=\pi$} ^{1%}
P_{pp}/P_0	2.0 %	2.0 %	1.0 %	1.0 %
ϕ	0	π	0	π

Table 8: Test cases with acoustic modulation.

6.2 Calculated flow dynamics and experimental data

When acoustic modulations are in phase, pressure fluctuations are produced at the injector outlet at the modulation frequency. This leads to oscillations of the axial velocity at the imposed frequency. Such variations in the longitudinal velocity induce a periodic shedding of ring-like patterns (Fig. 20). Structures are created behind the inner lip and in the outer mixing layer. These structures develop in an axi-symmetric fashion producing annular vortices. The vortices produced in the inner jet lip entrain fluid from the inner jet, involving mass from the inner jet in the vortex roll-up. These results are qualitatively consistent with experimental observations shown in Fig. 22(a), where a varicose motion is clearly identifiable. When acoustic perturbations are in phase-opposition (Fig. 21),

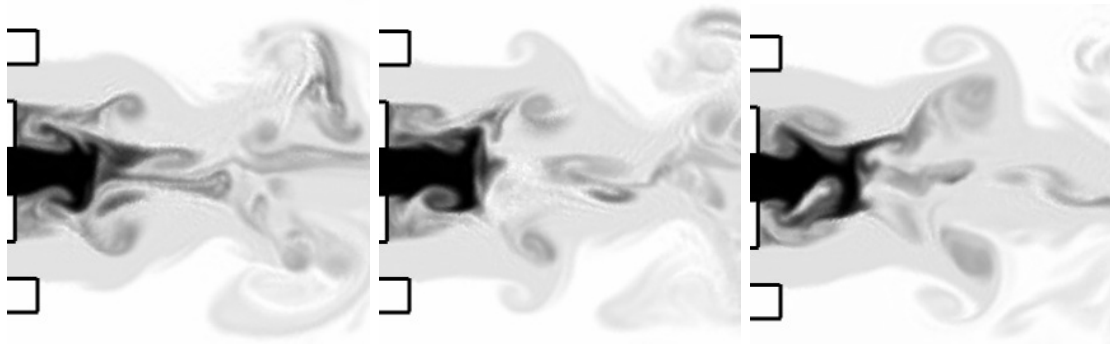


Figure 20: Case “N6 _{$\phi=0$} ^{2%}” ($J=3.05$). Longitudinal slices of density (white: 60 kg m^{-3} ; black: maximum ; logarithmic scale). These images correspond to three successive times in one period.

the resulting transverse velocity perturbation induces a sinusoidal motion, as observed experimentally in Fig. 22(b); and vortices are shed in an asymmetric fashion.

The centerline density and axial velocity are plotted in Fig. 23. Acoustic perturbations significantly reduce the dense core length and increase the amplitude of the low



Figure 21: Case “N6 $_{\phi=\pi}^{2\%}$ ” ($J=3.05$). Longitudinal slices of density (white: 60 kg m^{-3} ; black: maximum ; logarithmic scale). These images correspond to three successive times in one period.

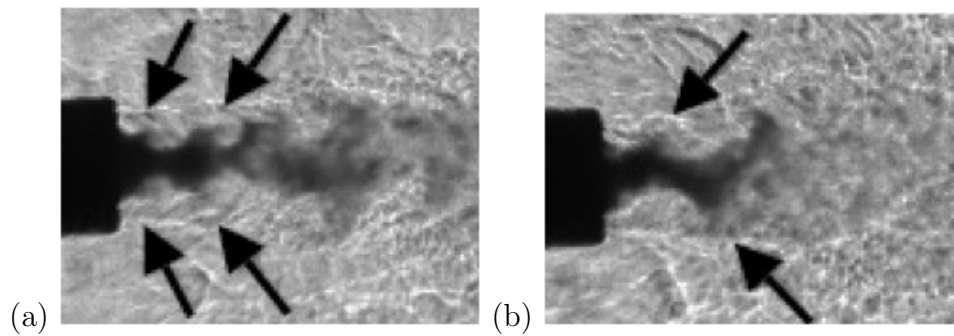


Figure 22: Experimental shadowgraphs for case “N6”. (a) Acoustic modulation is in phase, (b) Acoustic modulation is in phase-opposition.

velocity region just behind the central jet. Characteristic length ratios between acoustically perturbed cases and the reference case “N6” are given in Tab. 9. These ratios are in agreement with experimental measurements. It is interesting to note that the cases corresponding to phase opposition produce the shortest dense core. It is also found that multiplication of the perturbation amplitude by a factor of two does not lead to a proportional reduction of the dense core.

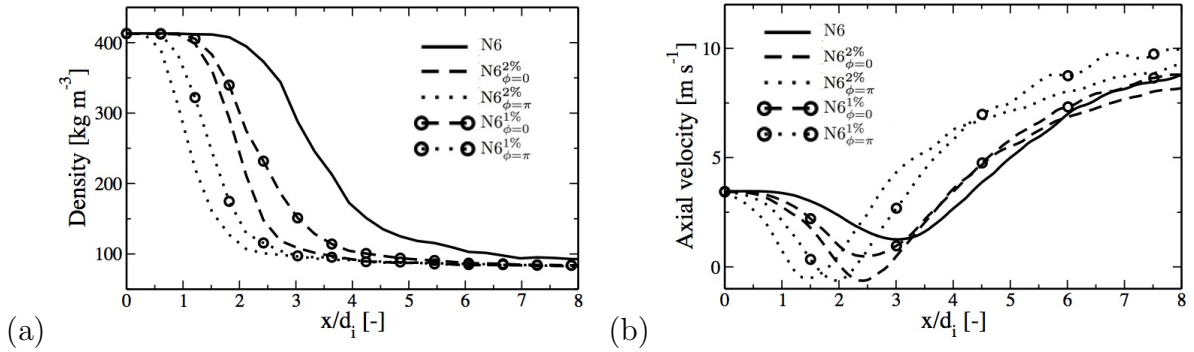


Figure 23: (a) Density profile on the centerline. (b) Axial velocity profile on the centerline.

Case	N6 ^{2%} _{φ=0}	N6 ^{2%} _{φ=π}	N6 ^{1%} _{φ=0}	N6 ^{1%} _{φ=π}
$l_{\rho}^{0.5}/l_{\rho,noac}^{0.5}$	0.60	0.34	0.70	0.45
$l_{\rho}^{0.1}/l_{\rho,noac}^{0.1}$	0.53	0.36	0.66	0.45
Experiments	-	-	0.68	0.55

Table 9: Influence of acoustic modulations on the characteristic length in case “N6”.

6.3 Spectral analysis of acoustic modulation effects

The response of the flow to the external modulation may now be discussed by examining the spectral content of velocity fluctuations. This is done by plotting spectral maps of these fluctuations along three axial lines in the flow. The first (line C) corresponds to the centerline, the second (line B) is centered on the lip, the third (line A) is centered on the outer jet annulus (see Fig. 24).

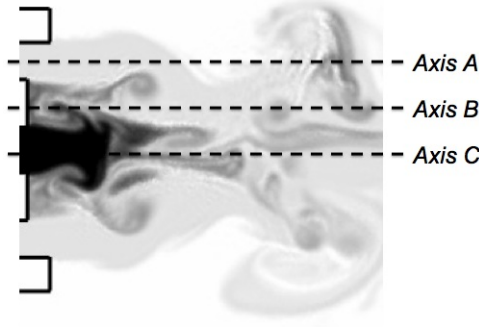


Figure 24: Case “N6 $_{\phi=0}^{2\%}$ ” ($J=3.05$). Positions of the three axial lines used in the spatial spectral analysis.

6.3.1 Case “N6 $_{\phi=0}^{2\%}$ ”

In-phase excitation induces axial velocity modulations on the centerline. This is clearly seen in Fig. 25(a), 26(a) and 27(a), where the 3 000 Hz fluctuations are well retrieved. The amplitude of the axial velocity fluctuation is nevertheless very low in the high-density region (Fig. 28), in the potential core of the inner jet ($x < 1.05 d_i$, defined by the region along the centerline axis where $\rho > 0.99\rho_i$, see Fig. 23(a)). This region of the flow is less affected by the axial modulation than the surround streams. The response of the jets to this modulation is determined by examining the transverse velocity. Both the outer jet and the flow behind the inner lip show a strong response at 3 000 Hz (Fig. 25(b) and 26(b)). It means that the axial perturbation promotes a destabilization of these jets and vortex roll-up at the same frequency. This is not the case along the inner jet centerline, where the transverse response at 3 000 Hz is not distinguishable (Fig. 27(b)). Since the geometry and the perturbation are both axisymmetric around this axis, such a velocity motion is naturally limited. The dominant frequency after the potential core ($x > 1.05 d_i$) is close to 1 000 Hz. The spectral content of the inner jet is shown in Fig. 28 at $x = d_i$, at the end of the potential core. The axial velocity is dominated by the modulation at 3 000 Hz, with a low amplitude, but also features a lower frequency component around 1 200 Hz. In contrast with the outer jet, the radial velocity responds at half of the imposed frequency (around 1 500 Hz). These fluctuations are nevertheless small compared to those

measured in the gaseous part of the flow. As a consequence, the high density part of the inner jet seems to be virtually insensitive to the acoustic modulation. The frequency that dominates at the end of the potential core is close to half of the modulation frequency. This frequency is also observed in the analysis of density fluctuations.

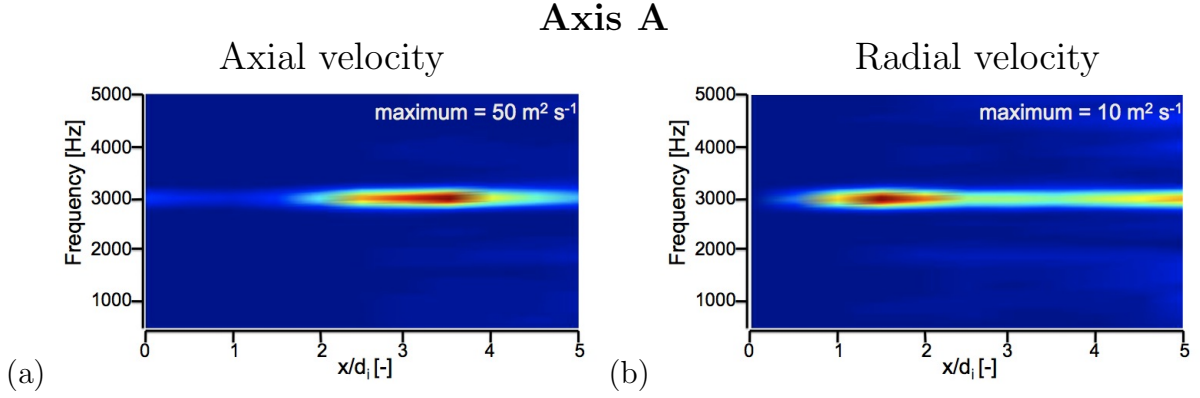


Figure 25: Case “N6 _{$\phi=0$} ^{2%}” ($J=3.05$). Spectral map along line A ($r = d_i/2 + l_i + h_e/2$). (a) Axial velocity, (b) Radial velocity.

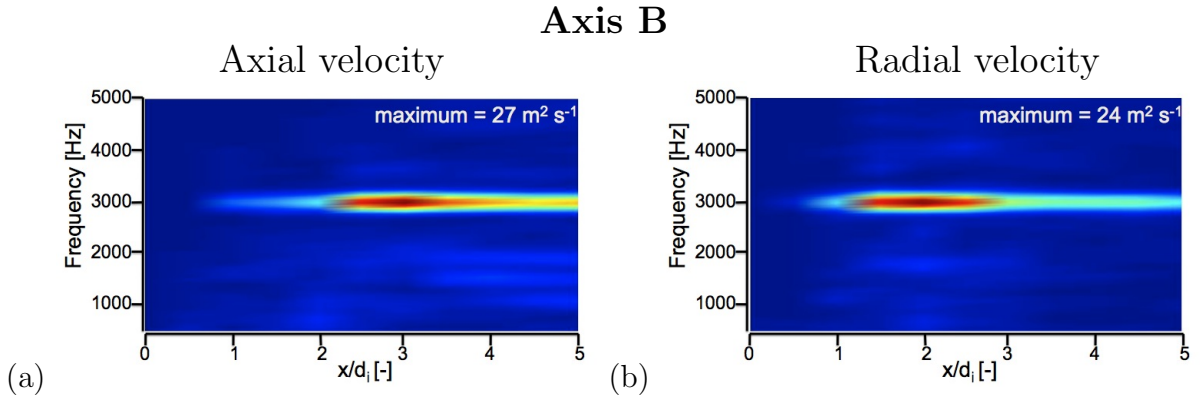


Figure 26: Case “N6 _{$\phi=0$} ^{2%}” ($J=3.05$). Spectral map along line B ($r = d_i/2 + l_i/2$). (a) Axial velocity and (b) Radial velocity.

6.3.2 Case “N6 _{$\phi=\pi$} ^{2%}”

A transverse velocity modulation is again applied at 3 000 Hz, but the phase is now equal to π . As in the previous case “N6 _{$\phi=0$} ^{2%}”, this transverse modulation affects all the jets as shown in Fig. 29 (b), 30 (b) and 31 (b). The amplitude of this transverse perturbation is much lower in the high density part of the inner jet (Fig. 32 and 31(b) for $x < d_i$).

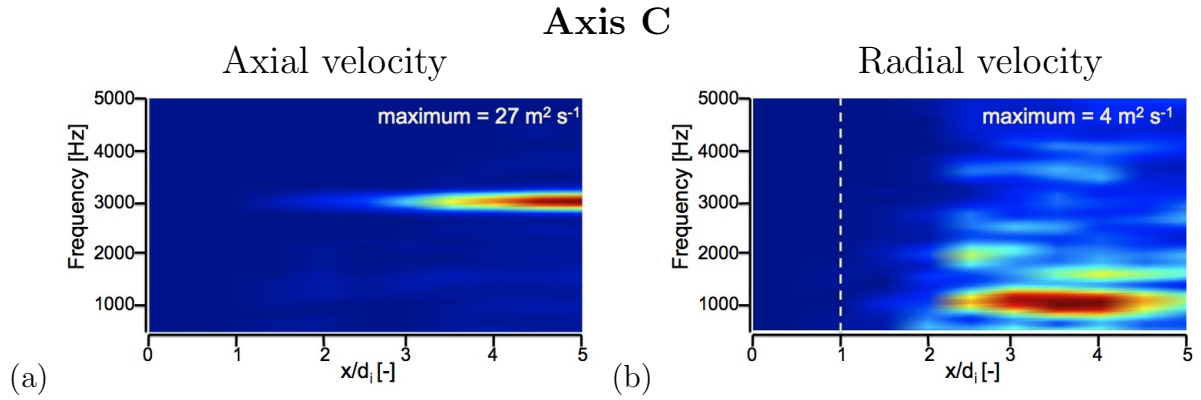


Figure 27: Case “N6 $_{\phi=0}^{2\%}$ ” ($J = 3.05$). Spectral map along line C ($r = 0$). (a) Axial velocity, (b) Radial velocity. The dashed line represents the axial position at which a power spectral density is shown in Fig. 28.

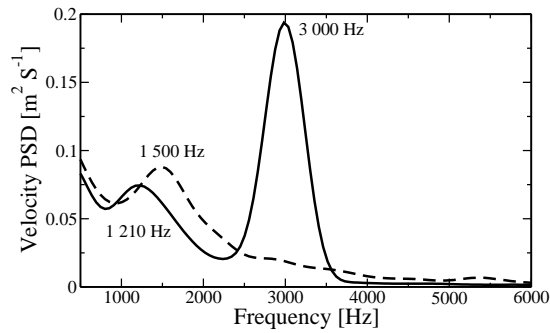


Figure 28: Case “N6 $_{\phi=0}^{2\%}$ ” ($J = 3.05$). Power spectral density of axial (—) and radial (- -) velocity in the inner jet centerline at $x = d_i$ (end of the potential core).

Axial velocity perturbations are induced in the outer jet and behind the inner lip (Fig. 29(a) and 30(a)), associated with vortex roll-up at the same frequency. Again, the inner jet is essentially unaffected, since the measured amplitudes are much lower than for the two other cases (Fig. 31(a)). This stream is dominated by an intermediate frequency. A component at 1 500 Hz is observed just at the inner injector exit. This is confirmed in Fig. 32, where the transverse modulation at 3 000 Hz is visible, but leads to a longitudinal response of the jet close to 1 500 Hz. Even though this frequency is clearly identifiable in Fig. 31(a) and 32, its amplitude is lower than that measured behind the lip or in the outer jet. As previously observed for in-phase modulation, the sensitivity of the inner jet to the external modulation is limited. Again, the frequency which dominates at the end of the potential core ($x < 0.55 d_i$, see Fig. 23(a)) is close to half of the modulation frequency and is also observed in density fluctuations.

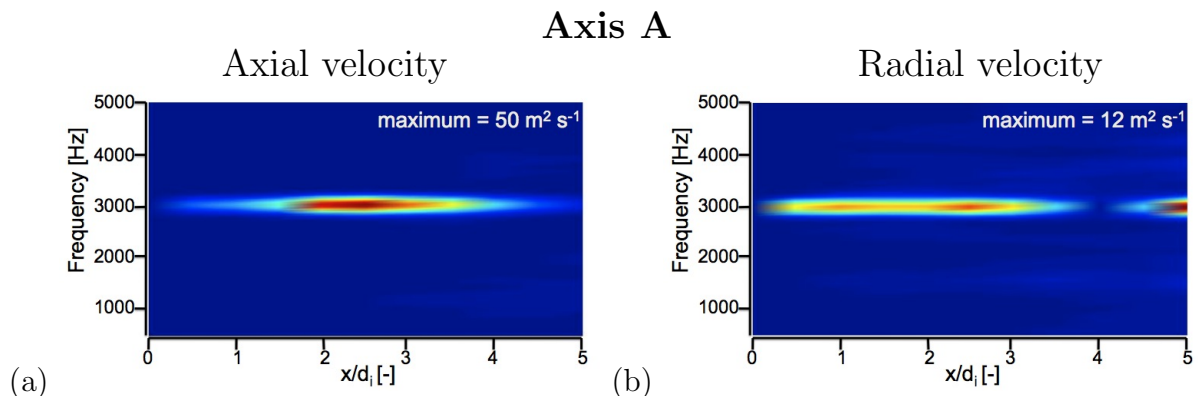


Figure 29: Case “N6 $_{\phi=\pi}^{2\%}$ ” ($J = 3.05$). Spectral map along line A ($r = d_i/2 + l_i + h_e/2$). (a) Axial velocity and (b) Radial velocity.

6.4 Discussion

It is found that the inner jet, when submitted to an acoustic modulation at 3 000 Hz, exhibits fluctuations at the subharmonic frequency of 1 500 Hz. This may be explained by considering the stability properties of the central jet and by analyzing the acoustic transmission from the outer medium into the high density region.

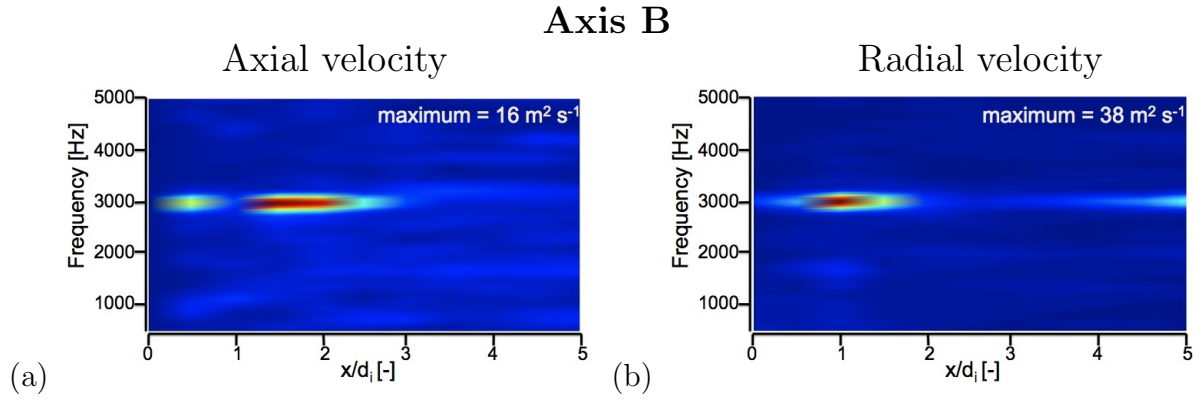


Figure 30: Case “N6 $_{\phi=\pi}^{2\%}$ ” ($J=3.05$). Spectral map along line B ($r = d_i/2 + l_i/2$). (a) Axial velocity and (b) Radial velocity.

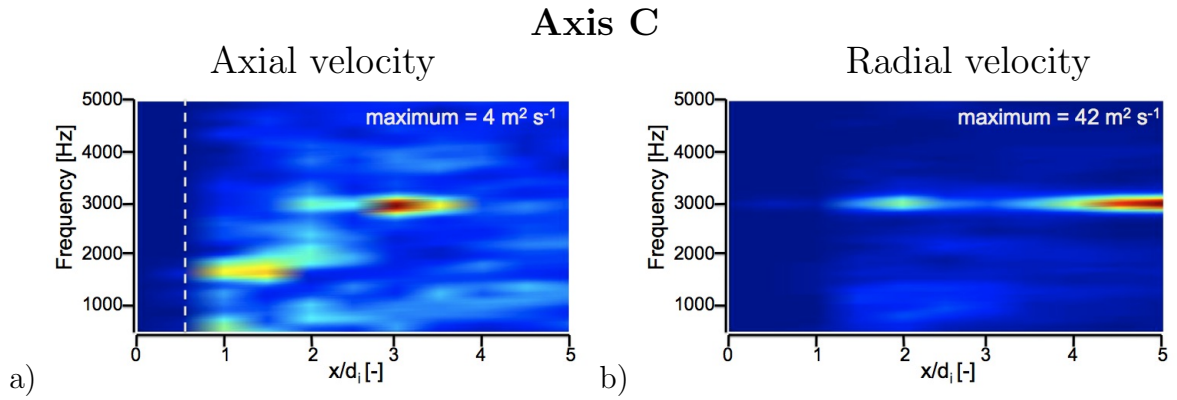


Figure 31: Case “N6 $_{\phi=\pi}^{2\%}$ ” ($J=3.05$). Spectral map along line C ($r = 0$). (a) Axial velocity and (b) Radial velocity. The dashed line represents the axial position at which a power spectral density is shown in Fig. 32.

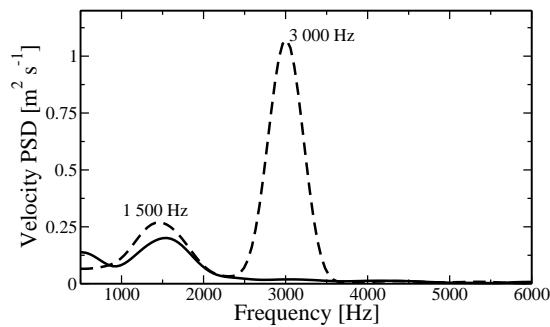


Figure 32: Case “N6 $_{\phi=\pi}^{2\%}$ ” ($J=3.05$). Power spectral density of axial (—) and radial (---) velocity on the inner jet centerline at $x = 0.5d_i$ (end of the potential core).

It is first interesting to situate the modulation frequency with respect to the range of unstable frequencies characterizing the jet and, more specifically, with respect to the preferred frequency of the inner jet. It is known (see for example Birbaud et al. [3] and references in this article) that when the modulation frequency is well above the preferred mode frequency, the flow is not affected by an external acoustic modulation. This is best expressed in terms of a Strouhal number which can be calculated by considering the acoustic modulation frequency, the characteristic length and velocity associated with each jet. The resulting “acoustic” Strouhal numbers are given in Tab. 10. While St_{ac}^e and St_{ac}^l are lower or close to the natural Strouhal number of the flow for case “N6”, St_{ac}^i is higher than the one measured previously without modulation. As a consequence, the jet does not respond to the modulation frequency, but oscillates at a subharmonic frequency (1 500Hz) which is close to the preferred frequency measured previously in the absence of acoustic modulation (Fig. 14).

$St = (f_{ac}l)/u$	length scale l	charac. vel. u	value
St_{ac}^e	h_e (0.41 mm)	u_e	0.087
St_{ac}^l	l_i (0.54 mm)	u_e	0.115
St_{ac}^i	d_i (0.51 mm)	u_i	0.45

Table 10: Definition of the Strouhal numbers used in this study. f represents the modulation frequency (3 000 Hz).

Another possible explanation of the absence of modulation at the imposed frequency may be obtained by considering the change in acoustic impedance between the outer stream and the inner jet. It is known that a large impedance mismatch reduces the transmission of waves across the interface. Acoustic impedances gathered in Tab. 11 indicate that a large variation takes place at the inner jet boundary. Under these circumstances acoustic wave transmission into the jet is reduced, explaining the absence of the modulation imposed to the system from the outer region.

The previous arguments provide some clues on the observed response of the coaxial flow to an externally imposed transverse acoustic motion. The strong reduction of the

Conditions	Impedance ($Z = \rho c$)
Chamber	17 701
Outer jet	19 663
Inner jet	98 700

Table 11: Specific acoustic impedance in the chamber, inner and outer jets.

inner jet length is certainly linked to the strong response of the outer jet to the acoustic modulation, which is not observed for the inner stream. The large vortices generated in the annular jet in turn enhance mixing between the outer and inner jets, and thus enhance mixing of the inner fluid with its surroundings, leading to a reduction of the dense core length.

7 Conclusion

The structure of non-reactive transcritical and supercritical jets is investigated by examining the flow formed by a coaxial injector operating at high pressure. This unit injects low temperature dense nitrogen surrounded by an outer stream of higher temperature nitrogen. The analysis relies on large eddy simulations which are compared with experimental results. The natural development of the coaxial flow is examined for a set of momentum flux ratios. It is shown that the flow patterns observed experimentally are suitably retrieved and that a good correspondence between experimental results and simulations is obtained. It is shown in particular that when the momentum flux ratio exceeds a critical value, the central jet is terminated in an abrupt fashion at a short distance from the injector exhaust. Calculations indicate that this is linked to the formation of a recirculation region located at a short distance from the injection section. This study is complemented with a spectral analysis of the velocity components in the injector nearfield. It is shown that the frequency content is governed by Strouhal numbers which follow standard rules for jets and wakes. The effect of an external acoustic modulation is then investigated by imposing in-phase and out-of-phase perturbations at the boundaries

of the domain. This is used to study the effect of transverse waves on the dark core in the jet. A strong reduction of the jet length is clearly observed, both in experiment and numerics. The spectral content of fluctuations in the coaxial streams is analyzed. In the case considered which corresponds to a Strouhal number (based on the inner jet velocity and diameter) about equal to twice the Strouhal number corresponding to the preferred mode of the jet, it is found that the inner jet responds with a limited amplitude to the external modulation but features a subharmonic motion at half of the modulation frequency. In contrast, the gaseous part of the flow is strongly perturbed by the acoustic modulation. Large scale vortices are released from the outer annulus at the modulation frequency. It is suggested that the relative insensitivity of the inner flow is linked to the fact that the frequency is above the range of unstable frequencies of the central jet. It is also found that the specific acoustic impedance of the central jet is much higher than that corresponding to the surrounding stream and that this may explain why the modulation is not transmitted to the central core.

Acknowledgments

This research was carried out with the partial support from EORD in the framework of contract FA8655-09-1-3114 and AFOSR under Mitat Birkan, program manager. The AVBP solver used for this study has been developed at Cerfacs. This work was granted access to the HPC resources of CINES under the allocation 2010 - 026176 made by GENCI (Grand Equipement National de Calcul Intensif).

References

- [1] J. Bellan. Supercritical (and subcritical) fluid behavior and modeling: drops, streams, shear and mixing layers, jets and sprays. *Progress in Energy and Combustion Science*, 26:329–366, 2000.

- [2] J. Bellan. Theory, modeling and analysis of turbulent supercritical mixing. *Combustion Science and Technology*, 178(1):253–281, 2006.
- [3] A. L. Birbaud, D. Durox, S. Ducruix, and S. Candel. Dynamics of free jets submitted to upstream acoustic modulations. *Physics of Fluids*, 19:013602, 2007.
- [4] R. Branam and W. Mayer. Characterisation of cryogenic injection at supercritical pressure. *Journal of Propulsion and Power*, 19(3):342–355, May-June 2003.
- [5] S. Candel, M. Juniper, G. Singla, P. Scoufflaire, and C. Rolon. Structure and dynamics of cryogenic flames at supercritical pressure. *Combustion Science and Technology*, 178:161–192, 2006.
- [6] I. Celik, A. Smirnov, and J. Smith. Appropriate initial and boundary conditions for LES of a ship wake. In *Proceedings of the 3rd ASME/JSME Joint Fluids Engineering Conference*, volume FEDSM99-7851, San Francisco, California, USA, 1999.
- [7] M.W. Chase. *NIST-JANAF thermochemical tables*. American Institute of Physics,-1, 1998.
- [8] B. Chehroudi and D. Talley. Interaction of acoustic waves with a cryogenic nitrogen jet at sub- and supercritical pressures. In *40th AIAA, Aerospace Science Meeting & Exhibit, Reno, Nevada*, January 2002.
- [9] B. Chehroudi, D. Talley, and E. Coy. Visual characteristics and initial growth rate of round cryogenic jets at subcritical and supercritical pressures. *Physics of Fluids*, 14(2):850–861, february 2002.
- [10] C. J. Chen and W. Rodi. *Vertical turbulent buoyant jets: A review of experimental data*. Pergamon Press, 1980.
- [11] G.C. Cheng and R. Farmer. Real fluid modeling of multiphase flows in liquid rocket engine combustors. *Journal of Propulsion and Power*, 22(6):1373–1381, 2006.

- [12] T.H. Chung, M. Ajlan, L.L. Lee, and K.E. Starling. Generalized multiparameter correlation for nonpolar and polar fluid transport properties. *Industrial & Engineering Chemistry Research*, 27(4):671–679, 1988.
- [13] D. W. Davis and B. Chehroudi. Measurements in an acoustically-driven coaxial jet under sub-, near-, and supercritical conditions. *Journal of Propulsion and Power*, 23(2):364–374, 2007.
- [14] D.W. Davis, B. Chehroudi, and I. Sorensen. Measurements in an acoustically driven coaxial jet under supercritical conditions. In *43rd AIAA Aerospace Sciences Meeting & Exhibit*, pages 10–13, 2005.
- [15] R. Dehoff. *Thermodynamics in Materials Science*. Taylor & Francis, second edition edition, 2006.
- [16] F.X. Demoulin, S. Zurbach, and A. Mura. High-Pressure Supercritical Turbulent Cryogenic Injection and Combustion: A Single-Phase Flow Modeling Proposal. *Journal of propulsion and power*, 25(2), 2009.
- [17] N. Guezennec and T. Poinso. Acoustically non-reflecting and reflecting boundary conditions for injection of vortical flows in compressible solvers. *American Institute of Aeronautics and Astronautics Journal*, 2009.
- [18] J. Gullbrand and F. K. Chow. The effect of numerical errors of turbulence models in large eddy simulations of channel flow, with and without explicit filtering. *Journal of Fluid Mechanics*, 495:323–341, 2003.
- [19] M. Habiballah, M. Orain, F. Grisch, L. Vingert, and P. Gicquel. Experimental studies of high-pressure cryogenic flames on the Mascotte facility. *Combustion Science and Technology*, 178(1):101–128, 2006.
- [20] J.O. Hirschfelder, C.F. Curtiss, and R.B. Bird. *Molecular theory of gases and liquids*. Wiley New York, 1954.

- [21] A. G. Kravchenko and P. Moin. On the effect of numerical errors in large eddy simulations of turbulent flows. *Journal of Computational Physics*, 131:310–322, 1996.
- [22] JC Lasheras, E. Villermaux, and EJ Hopfinger. Break-up and atomization of a round water jet by a high-speed annular air jet. *Journal of Fluid Mechanics*, 357:351–379, 1998.
- [23] E.W. Lemmon, M.O. McLinden, and D.G. Friend. Thermophysical properties of fluid systems. In Eds. P.J. Linstrom and W.G. Mallard, editors, *NIST Chemistry WebBook, NIST Standard Reference Database 69*, Gaithersburg, MD, first retrieved May 2007. National Institute of Standards and Technology.
- [24] I. A. Leyva, J. Rodriguez, B. Chehroudi, and D. Talley. Preliminary results on coaxial jet spread angles and the effects of variable phase transverse acoustic fields. In *46th AIAA Aerospace Sciences Meeting and Exhibit, Reno, Nevada, Jan. 7-10*, volume AIAA-2008-950, 2008.
- [25] I.A. Leyva, B. Chehroudi, and D. Talley. Dark Core Analysis of Coaxial Injectors at Sub-, Near-, and Supercritical Conditions in a Transverse Acoustic Field. In *43rd AIAA/ASME/SAE/ASEE Joint Propulsion Conference and Exhibit, Cincinnati, OH, July 8-11*, volume AIAA-2007-5456, 2007.
- [26] T. Liu, N. Zong, and V. Yang. Dynamics of Shear-Coaxial Cryogenic Nitrogen Jets with Acoustic Excitation under Supercritical Conditions. In *44th AIAA Aerospace Sciences Meeting and Exhibit, 9 - 12 January 2006, Reno, Nevada, AIAA 2006-75*, 2006.
- [27] M. Masquelet, S. Menon, Y. Jin, and R. Friedrich. Simulation of unsteady combustion in a LOX-GH2 fueled rocket engine. *Aerospace Science and Technology*, 13(8):466–474, 2009.

- [28] S. Matsuyama, J. Shinjo, S. Ogawa, and Y. Mizobuchi. Large Eddy Simulation of LOX/GH2 Shear-Coaxial Jet Flame at Supercritical Pressure. In *48th AIAA Aerospace Sciences Meeting, Orlando, Florida*, January 2010.
- [29] W. Mayer, J. Tellar, R. Branam, G. Schneider, and J. Hussong. Raman measurement of cryogenic injection at supercritical pressure. *Heat and Mass Transfer*, 39:709–719, 2003.
- [30] W.O.H. Mayer and R. Branam. Atomization characteristics on the surface of a round liquid jet. *Experiments in Fluids*, 36:528–539, 2004.
- [31] H. Meng and V. Yang. A unified treatment of general fluid thermodynamics and its application to a preconditioning scheme. *Journal of Computational Physics*, 189(1):277–304, 2003.
- [32] Y. Mery, S. Ducruix, P. Scoufflaire, and S. Candel. Injection coupling with high amplitude transverse modes: Experimentation and simulation. *Comptes Rendus Mécanique*, 337(6-7):426–437, 2009.
- [33] R. S. Miller, K. G. Harstad, and J. Bellan. Direct numerical simulation of supercritical fluid mixing layers applied to heptane-nitrogen. *Journal of Fluid Mechanics*, 436:1–39, 2001.
- [34] V. Moureau, G. Lartigue, Y. Sommerer, C. Angelberger, O. Colin, and T. Poinsot. High-order methods for DNS and LES of compressible multi-component reacting flows on fixed and moving grids. *Journal of Computational Physics*, 202(2):710–736, 2005.
- [35] F. Nicoud and F. Ducros. Subgrid-scale stress modelling based on the square of the velocity gradient. *Flow, Turbulence and Combustion*, 62(3):183–200, 1999.
- [36] J. C. Oefelein and V. Yang. Modeling high-pressure mixing and combustion processes in liquid rocket engines. *Journal of Propulsion and Power*, 14(5):843–857, 1998.

- [37] J.C. Oefelein. Thermophysical characteristics of shear-coaxial LOX-H₂ flames at supercritical pressure. *Proceedings of the Combustion Institute*, 30(2):2929–2937, 2005.
- [38] J.C. Oefelein. Mixing and combustion of cryogenic oxygen-hydrogen shear-coaxial jet flames at supercritical pressure. *Combustion Science and Technology*, 178(1):229–252, 2006.
- [39] N. Okong’o and J. Bellan. Consistent boundary conditions for multicomponent real gas mixtures based on characteristic waves. *Journal of Computational Physics*, 176:330–344, 2002.
- [40] M. Oswald and M. M. Micci. Spreading angle and centerline variation of density of supercritical nitrogen jets. *Atomization and Sprays*, 11:91–106, 2002.
- [41] M. Oswald and A. Schik. Supercritical nitrogen free jet investigated by spontaneous raman scattering. *Experiments in Fluids*, 27:497–506, 1999.
- [42] M. Oswald, A. Schik, M. Klar, and W. Mayer. Investigation of coaxial LN₂-GH₂-injection at supercritical pressure by spontaneous Raman scattering. AIAA 99-2887. In *35th Joint Propulsion Conference, Los Angeles, CA*, 1999.
- [43] M. Oswald, J. J. Smith, R. Branam, J. Hussong, A. Shick, B. Chehroudi, and D. Talley. Injection of fluids into supercritical environments. *Combustion Science and Technology*, 178:49–100, 2006.
- [44] N. Otsu. A threshold selection method from gray-level histograms. *Automatica*, 11:285–296, 1975.
- [45] D. Peng and D. B. Robinson. A new two-constant equation of state. *Ind. Eng. Chem. Fundam.*, 15:59–64, 1976.
- [46] T. Poinso and S. Lele. Boundary conditions for direct simulations of compressible viscous flows. *Journal of Computational Physics*, 101(1):104–129, 1992.

- [47] B. E. Poling, J. M. Prausnitz, and J. P. O'Connell. *The properties of gases and liquids*. McGraw-Hill, fifth edition, 2001.
- [48] L. Pons, N. Darabiha, S. Candel, T. Schmitt, and B. Cuenot. The structure of multidimensional strained flames under transcritical conditions. *Comptes rendus-Mécanique*, 337(6-7):517–527, 2009.
- [49] M.M. Poschner and M. Pfitzner. CFD-Simulation of the injection and combustion of LOX and H₂ at supercritical pressures. In *Proceedings of the European Combustion Meeting 2009*, 2010.
- [50] L. Quartapelle and V. Selmin. High-order Taylor-Galerkin methods for non-linear multidimensional problems., 1993.
- [51] H. Rehab, E. Villermaux, and EJ Hopfinger. Flow regimes of large-velocity-ratio coaxial jets. *Journal of Fluid Mechanics*, 345:357–381, 1997.
- [52] C. Rey, S. Ducruix, and S. Candel. A method for the transverse modulation of reactive flows with application to combustion instability. *Combustion Theory and Modelling*, 9:5–22, 2005.
- [53] F. Richecoeur, P. Scouflaire, S. Ducruix, and S. Candel. High-frequency transverse acoustic coupling in a multiple-injector cryogenic combustor. *Journal of propulsion and power*, 22(4):790–799, 2006.
- [54] J. Rodriguez, J. Graham, I. Leyva, and D. Talley. Effect of Variable Phase Transverse Acoustic Fields on Coaxial Jet Forced Spread Angles. In *47th AIAA Aerospace Sciences Meeting including The New Horizons Forum and Aerospace Exposition, Orlando, Florida, Jan. 5-8*, volume AIAA-2009-231. American Institute of Aeronautics and Astronautics, 1801 Alexander Bell Dr., Suite 500 Reston VA 20191-4344 USA,, 2009.

- [55] J. Rodriguez, I. Leyva, J. Graham, and D. Talley. Mixing Enhancement of Liquid Rocket Engine Injector Flow. In *45th AIAA/ASME/SAE/ASEE Joint Propulsion Conference and Exhibit, Denver, Colorado, Aug. 2-5*, volume AIAA-2009-5143, 2009.
- [56] A. Roy and C. Segal. Experimental Study of Fluid Jet Mixing at Supercritical Conditions. *Journal of Propulsion and Power*, 26(6), 2010.
- [57] T. Schmitt, Y. Méry, M. Boileau, and S. Candel. Large-Eddy Simulation of oxygen/methane flames under transcritical conditions. *Proceedings of the Combustion Institute*, 2010.
- [58] T. Schmitt, L. Selle, B. Cuenot, and T. Poinso. Large-Eddy Simulation of transcritical flows. *Comptes Rendus Mécanique*, 337(6-7):528–538, 2009.
- [59] T. Schmitt, L. Selle, A. Ruiz, and B. Cuenot. Large-Eddy Simulation of Supercritical-Pressure Round Jets. *AIAA journal*, 48(9), 2010.
- [60] T. Schönfeld and T. Poinso. Influence of boundary conditions in LES of premixed combustion instabilities. In *Annual Research Briefs*, pages 73–84. Center for Turbulence Research, NASA Ames/Stanford Univ., 1999.
- [61] C. Segal and SA Polikhov. Subcritical to supercritical mixing. *Physics of Fluids*, 20:052101, 2008.
- [62] L. Selle and T. Schmitt. Large-eddy simulation of single-species flows under supercritical thermodynamic conditions. *Combustion Science and Technology*, 182(4):392–404, 2010.
- [63] L.C. Selle, N.A. Okong’o, J. Bellan, and K.G. Harstad. Modelling of subgrid-scale phenomena in supercritical transitional mixing layers: an a priori study. *Journal of Fluid Mechanics*, 593:57–91, 2007.
- [64] G. Singla. *Etude des Flammes Cryotechniques Oxygène Liquide/Méthane à Haute Pression*. PhD thesis, Ecole Centrale de Paris, 2005.

- [65] G. Singla, P. Scoufflaire, C. Rolon, and S. Candel. Planar laser-induced fluorescence of OH in high-pressure cryogenic LOx/GH₂ jet flames. *Combustion and Flame*, 144(1-2):151–169, 2006.
- [66] A. Smirnov, S. Shi, and I. Celik. Random flow generation technique for large eddy simulations and particle-dynamics modeling. *Trans. ASME. Journal of Fluids Engineering*, 123:359–371, 2001.
- [67] J. J. Smith, G. Schneider, D. Suslov, M. Oswald, and O. Haidn. Steady-state high pressure lox/h₂ rocket engine combustion. *Aerospace Science and Technology*, 11:39–47, 2007.
- [68] E.S. Taskinoglu and J. Bellan. A posteriori study using a DNS database describing fluid disintegration and binary-species mixing under supercritical pressure: heptane and nitrogen. *Journal of Fluid Mechanics*, 645:211–254, 2010.
- [69] E. Villermaux and H. Rehab. Mixing in coaxial jets. *Journal of Fluid Mechanics*, 425:161–185, 2000.
- [70] D. Wee, T. Yi, A. Annaswamy, and A.F. Ghoniem. Self-sustained oscillations and vortex shedding in backward-facing step flows: Simulation and linear instability analysis. *Physics of Fluids*, 16:3361–3373, 2004.
- [71] V. Yang. Modeling of supercritical vaporization, mixing, and combustion processes in liquid-fueled propulsion systems. *Proceedings of the Combustion Institute*, 28(1):925–942, 2000.
- [72] V. Yang. *Liquid rocket thrust chambers: aspects of modeling, analysis, and design*. Aiaa, 2004.
- [73] N. Zong. *Modeling and simulation of cryogenic fluid injection and mixing dynamics under supercritical conditions*. PhD thesis, The Pennsylvania State University, 2005.

- [74] N. Zong, H. Meng, S.-Y. Hsieh, and V. Yang. A numerical study of cryogenic fluid injection and mixing under supercritical conditions. *Physics of Fluids*, 16(12):4248–4261, 2004.
- [75] N. Zong and V. Yang. A numerical study of high-pressure oxygen/methane mixing and combustion of a shear coaxial injector. *AIAA paper*, 152, 2005.
- [76] N. Zong and V. Yang. Cryogenic fluid jets and mixing layers in transcritical and supercritical environments. *Combustion Science and Technology*, 178(1):193–227, 2006.
- [77] N. Zong and V. Yang. Near-field flow and flame dynamics of LOX/methane shear-coaxial injector under supercritical conditions. *Proceedings of the Combustion Institute*, 31(2):2309–2317, 2007.

A Injection conditions for the computed cases

Outer jet injection conditions

Case	T_e [K]	\dot{m}_e [g.s ⁻¹]	ρ_e [kg.m ⁻³]	u_e [m.s ⁻¹]	Re_e
N2	152	1.57	101	5.95	41 600
N6	183	2.69	73.1	14.1	64 800
N8	192	6.46	68.3	36.2	151 000

Table 12: Injection conditions corresponding to the cases “N2”, “N6” and “N8” for the **outer** jet. \dot{m} denotes the mass flow rate.

Inner jet injection conditions

Case	T_i [K]	\dot{m}_i [g.s ⁻¹]	ρ_i [kg.m ⁻³]	u_i [m.s ⁻¹]	Re_i
N2	117	0.289	590	2.4	15 000
N6	126	0.292	420	3.4	25 000
N8	128	0.295	220	6.6	52 000

Table 13: Injection conditions corresponding to the cases “N2”, “N6” and “N8” for the **inner** jet. \dot{m} denotes the mass flow rate.